nature portfolio

https://doi.org/10.1038/s41586-026-10844-6

Supplementary information

Electrodeposited self-assembled molecules for perovskite photovoltaics

In the format provided by the authors and unedited

Supporting Materials for

Electrodeposited self-assembled molecules for perovskite photovoltaics

Zhihui Xiong†, Xuanang Luo†, Fushen Tang†, Bohan Wang, Sen Yin, Yu Li, Zhangyu Yuan, Chenxi Peng, Shaohua Tong, Jialin Wu, Xingwang Kang, Ganlin Liu, Ying Wang, Youran Lin, Mingke Li, Yulong Li, Yuanyuan Shu, Wei Meng, Ning Li, Lei Ying**

Institute of Polymer Optoelectronic Materials and Devices, Guangdong Basic Research Center of Excellence for Energy and Information Polymer Materials, State Key Laboratory of Luminescent Materials and Devices, South China University of Technology, Guangzhou 510640, China.

†These authors contributed equally to this work.

Corresponding E-mail: N.L. ningli2022@scut.edu.cn; L.Y. msleiying@scut.edu.cn;

Supplementary Note 1: Synthesis and characterization of ^{18}O-2PACz

Materials

The reagents and starting materials are commercially available and were used as received without further purification. (2-(9H-carbazol-9-yl)ethyl)phosphonic acid (2PACz) was sourced from Dongguan Volt-Amp Optoelectronics Tech Co. Ltd. (China). Dimethylformamide (DMF), dichloromethane (DCM), 1,4-dioxane, $H_2{}^{18}O$ and dimethyl sulfoxide-d6 (DMSO-d6) were purchased from J&K Scientific. Phosphorus pentachloride, palladium(II) acetate and potassium carbonate were purchased from TCI.

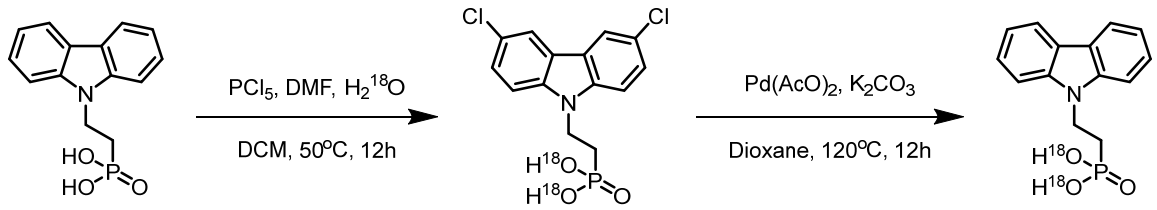

Scheme S1. Synthetic route of ^{18}O-2PACz.

The synthesis of (2-(3,6-dichloro-9H-carbazol-9-yl)ethyl)phosphonic-$^{18}O_2$ acid: To an oven-dried 50 mL flask was added (2-(9H-carbazol-9-yl)ethyl)phosphonic acid (450 mg, 1.63 mmol), phosphorus pentachloride (1.70 g, 8.17 mmol, 5 eq.), dimethylformamide (DMF) (1.20 mL, 16.35 mmol), and $H_2{}^{18}O$ (900 mg, 44.96 mmol, 27.50 eq.). An appropriate amount of dichloromethane (DCM) was added to assist in dissolution. The flask was filled with nitrogen, and the mixture was stirred at 50 °C for 12 hours. Upon completion of the reaction, the solvent was removed by rotary evaporation. The residue was dissolved in methanol, and added to water to precipitate a solid. The solid was filtered and recrystallized using a mixture of dichloromethane and petroleum ether to get 200 mg crude product. The crude product was filtered, dried under vacuum, and directly used for the next step.

The synthesis of (2-(9H-carbazol-9-yl)ethyl)phosphonic-$^{18}O_2$ acid: To an oven-dried 50 mL round-bottom flask was added the crude (2-(3,6-dichloro-9H-carbazol-9-yl)ethyl)phosphonic-$^{18}O_2$ acid (50 mg), palladium(II) acetate (97 mg, 430.88 μmol), and potassium carbonate (99 mg, 718.13 μmol). The reactants were then dissolved in 10 mL of 1,4-dioxane:water (2:1, v/v) mixture under nitrogen protection. The mixture was stirred at 120°C for 12 h. Upon completion

of the reaction, the solution was cooled to 25°C and HCl (0.01 mol L^{-1}, aq) was added to adjust the pH below 4.0. The liquid was then removed by rotary evaporation. The residue was dissolved in a mixture of dichloromethane and methanol (5:1, v/v). The solution was filtered, and activated carbon was added to decolorize the filtrate. The mixture was filtered again, and the filtrate was concentrated by rotary evaporation to obtain 20 mg white solid.

^{1}H NMR (400 MHz, DMSO-d_6) δ 8.16 (d, J = 7.8 Hz, 2H), 7.57 – 7.43 (m, 4H), 7.26 – 7.17 (m, 2H), 4.60 – 4.49 (m, 2H), 2.09 – 1.96 (m, 2H). HRMS-LCMS (m/z): $[M-H]^-$ Calcd. for ($C_{14}H_{13}NO^{18}O_2P$)： 278.07, found 278.07.

Supplementary Note 2: Characterization of electrodeposited layers and perovskite solar cells.

NMR measurements were performed on a Bruker AVANCE 400/500 spectrometer operating at 400 or 500 MHz, with tetramethylsilane (TMS) as the internal standard. UV–vis absorption spectra of spin-cast thin films on quartz were recorded on a Shimadzu UV-3600 UV–vis–NIR spectrometer. UPS and XPS were measured on an Axis Supra+ (Kratos), with Ag as the reference. Contact angles were measured on an OCA50 goniometer using deionized water and diiodomethane; surface energy was calculated by the Owens–Wendt–Rabel–Kaelble method. Field-emission scanning electron microscopy (FESEM) top-view and cross-section images were acquired on a Hitachi SU8600. Raman spectra were recorded on a Renishaw inVia microscope with a 50× objective at room temperature (λ = 532 nm; 0.5–10% laser power depending on sample). XRD patterns were collected on a PANalytical X'Pert Powder diffractometer. Temperature-dependent phase behavior was monitored using an Ocean Optics DT-MINI-2-GS under N_2 at 60 °C. Tapping-mode AFM images were obtained on a Bruker MultiMode 8. Kelvin probe force microscopy (KPFM) and conductive AFM (c-AFM) were performed on a Bruker Dimension Icon. Infrared AFM (IR-AFM) was acquired on an Anasys nanoIR3. ToF-SIMS images were collected on an ION TOF ToF SIMS 5-100. Photoluminescence quantum yield (PLQY) and time-resolved photoluminescence (TRPL) were measured on a FluoTime 300 fluorescence lifetime spectrometer.

Current–density–voltage (*J–V*) curves were measured with a Keithley 2400 source meter under 1-sun AM 1.5G illumination from a solar simulator (SS-F5, Enlitech). External quantum efficiency (EQE) was obtained using an Enlitech QE-R system, calibrated with a single-crystal Si photodetector prior to testing. TPV, TPC and impedance spectroscopy (EIS) were performed on the Platform for All-In-One Characterization of Solar Cells and OLEDs (PAIOS).

Supplementary Note 3: Characterization for electrochemical experiments and Cyclic voltammogram in a blank electrolyte solution.

Electrochemical experiments were performed on CH Instruments CHI 760D and Metrohm Autolab PGSTAT302N potentiostats in a three-electrode configuration under a dry, O_2-free atmosphere inside a nitrogen glove box (cells and electrolytes were Ar-purged prior to use). Acetonitrile (ACN) containing 0.1 M tetrabutylammonium hexafluorophosphate ($TBAPF_6$) served as the supporting electrolyte. ITO substrates were used as working electrodes. For film electrodeposition on ITO, a platinum (99.99%) plate was used as the counter electrode. A non-aqueous Ag/Ag^+ reference (RE-7, ALS) was employed with an internal reference solution of 0.01 M $AgNO_3$ + 0.1 M $TBAPF_6$ in ACN. Ferrocene (Fc) was measured before each experiment to calibrate the reference; unless otherwise noted, all potentials are reported vs Fc/Fc^+. Anhydrous ACN and EtOH (J&K Scientific) were used. $TBAPF_6$ (J&K Scientific) was recrystallized from ethanol three times and dried before use. Glassy carbon, Ti, and Pt electrodes were sourced from Tianjin Aida Hengsheng; carbon paper from Thermo Fisher Scientific; ITO glass from Guangzhou New Vision; $AgNO_3$ (99.999%) from Sigma-Aldrich.

For 2PACz electrodeposition, the electrolyte was ACN:EtOH = 1:10 (v/v) containing $TBAPF_6$ 0.1 M and 2PACz 1 mg mL^{-1}. Potentials were scanned from 0.4 to −2.15 V at 50 mV s^{-1} for 5 cycles (ITO working, Pt counter, Ag/Ag^+ reference). The 1:10 ACN:EtOH ratio was chosen to balance the solubilities of $TBAPF_6$ and 2PACz at these concentrations; lowering the ethanol fraction or increasing 2PACz concentration led to incomplete dissolution, aggregation, and degraded device performance. The optimal five-cycle endpoint was established by (i) the CV reduction feature associated with 2PACz interfacial formation becoming stationary by the fifth scan, (ii) IR-AFM coverage reaching a steady, uniform film from the fourth cycle onward, and (iii) device efficiencies becoming invariant beyond the fourth cycle. Consistent with these observations, five cycles were adopted as the standard. Oxygen-plasma pretreatment of ITO was tested and showed no measurable benefit for electrodeposited 2PACz; subsequent depositions were therefore carried out without plasma.

Blank-electrolyte CV on SAM-coated ITO (stability probe). ITO substrates bearing spin-coated or electrodeposited 2PACz were immersed as working electrodes in a blank electrolyte

(TBAPF$_6$ 0.1 M in ACN). Potentials were swept from 0 to 1.05 V (vs Fc/Fc$^+$) while monitoring the carbazole oxidation peak near 0.8 V. A progressive decrease of this peak over successive scans is consistent with a reduction in carbazole surface concentration at the electrolyte/electrode interface, which we attribute mainly to partial desorption into the electrolyte. This decay was prominent for spin-coated films and negligible for electrodeposited molecular layer under identical conditions.

Building on the electrodeposited 2PACz layer, DCPN was formed in ACN containing Cz–CN 1 mg mL^{-1} and TBAPF$_6$ 0.1 M by sweeping 0 to 1.05 V (vs Fc/Fc$^+$) at 50 mV s^{-1} for 8 cycles (ITO working, Pt counter). During the scan, surface-bound 2PACz underwent oxidative coupling with dissolved Cz–CN, yielding a dimeric carbazole-coupled molecular layer (DCPN). Two concurrent pathways can occur: coupling between surface-bound 2PACz and Cz–CN, and Cz–CN self-coupling in solution. After deposition, a brief ACN rinse removed self-coupled species without disturbing the anchored DCPN. The redox feature associated with dimer formation became stationary by the eighth cycle, and devices prepared beyond this point showed no further performance change; we therefore adopted eight cycles as standard condition for DCPN formation.

Supplementary Note 4: Absolute PLQY and time-resolved PL.

Absolute PLQY. Absolute photoluminescence was measured inside an integrating sphere using the substitution method with response-corrected spectra; a 450 nm laser diode served as the excitation source and its output was tuned by a stepwise attenuator. To approximate device-relevant excitation, the absorbed photon flux was adjusted to be comparable to the AM 1.5G above-gap photon flux for this material (Eg ≈ 1.56 eV), while remaining in the linear-response regime. After dark subtraction and system-response correction, the absolute external PLQY was obtained as the ratio of emitted photons to absorbed excitation photons according to the integrating-sphere protocol.

Transient PL decays were recorded on a FluoTime 300 spectrometer (TCSPC) with a 450 nm pulsed laser diode; the sampling step was 5 ns (time bin). The instrument response function (IRF) was measured on a scatterer and included by re-convolution fitting. The collection geometry and excitation density were kept comparable to the PLQY condition for cross-comparison.

Differential-lifetime analysis was performed on the TRPL decays of SAM/perovskite half stacks. The differential lifetime was calculated as $\tau(t) = -[dln\phi(t)/dt]^{-1}$, where $\phi(t)$ is the time-dependent PL intensity. To avoid numerical noise from direct differentiation of the raw data, the TRPL decays were first fitted using empirical triple-exponential functions with offsets. These fits were used only to obtain smooth derivatives and were not assigned to a specific physical recombination model.

Supplementary Note 5: Stability testing.

For stability assessment, inverted perovskite solar cells (PSCs) with the architecture of ITO/HTM/perovskite/C_{60}/BCP/Ag were used. The light intensity was calibrated using a calibrated silicon reference solar cell before the stability measurements.

For dark-storage ageing, encapsulated devices were stored in an environmental chamber at 85 °C and 50% relative humidity in the dark. The devices were taken out periodically for *J–V* measurements under standard one-sun conditions.

For operational stability, unencapsulated devices were measured under continuous maximum power point tracking at 65 °C under one-sun-equivalent illumination in a nitrogen-filled glovebox.

For open-circuit ageing, unencapsulated devices were held under open-circuit conditions at 65 °C under one-sun-equivalent LED illumination in a nitrogen-filled glovebox. *J–V* curves were measured periodically to evaluate PCE retention.

For all ageing tests, the reported temperature corresponds to the device-surface temperature measured using a thermocouple attached to a dummy device placed adjacent to the tested cells under the same ageing conditions. Average device characteristics and standard deviations were obtained from five cells for each condition.

Supplementary Note 6: Simulation.

The molecular structures for various SAMs were optimized by density functional theory (DFT) through Gaussian package, using the B3LYP-D3/6-31G** method and the IRI interaction is evaluated using Multiwfn and VMD on the basis of B3LYP-D3/tzvp[1,2]. The electron density difference (EDD) was obtained from DFT-optimized SAMs and calculated using GGA/PBE via CASTEP.

Supplementary Note 7: Shockley–Queisser-referenced loss accounting and pseudo *J–V* analysis.

The analysis was carried out by comparing the experimental device performance parameters with those of an ideal device in the detailed-balance limit. The relative loss contributions are primarily determined by four figures of merit, given by the following equation:

$$\frac{\eta_{real}}{\eta_{SQ}} = \frac{J_{SC}}{J_{SC}^{SQ}} \frac{V_{OC}^{real}}{V_{OC}^{SQ}} \frac{FF_0(V_{OC}^{real})}{FF_0(V_{OC}^{SQ})} \frac{FF_{real}}{FF(V_{OC}^{real})} \qquad \text{(Equation 1)}$$

Here, η_{real} and η_{SQ} represent the efficiencies of the real device and Shockley–Queisser (SQ) limited device, respectively, $V_{OC,real}$ and $V_{OC,SQ}$ from the real device and the device at the SQ limits, whereas $FF_0(V_{OC,real})$ and $FF_0(V_{OC,SQ})$ are calculated by an approximate equation:

$$FF_0(V_{OC}) = \left[\frac{qV_{OC}}{nk_BT} - \ln\left(\frac{qV_{OC}}{nk_BT} + 0.72\right)\right] / \left(\frac{qV_{OC}}{nk_BT} + 1\right) \qquad \text{(Equation 2)}$$

Where q denotes the elementary charge, n is the ideality factor, k_B is the Boltzmann constant, and T is the temperature.

The non-radiative voltage loss from the absolute photoluminescence quantum yield (PLQY) is calculated as:

$$\Delta V_{OC}^{nonrad} = -\frac{k_BT}{q} \ln(PLQY) \qquad \text{(Equation 3)}$$

To illustrate the losses arising from non-radiative and transport processes, pseudo *J–V* curves were constructed using the ideal-diode relation:

$$J(V) = J_{ph} - J_0\left[exp\left(\frac{qV}{nk_BT}\right) - 1\right], \quad J_0 = \frac{J_{ph}}{exp\left(\frac{qV_{OC}}{nk_BT}\right) - 1} \qquad \text{(Equation 4)}$$

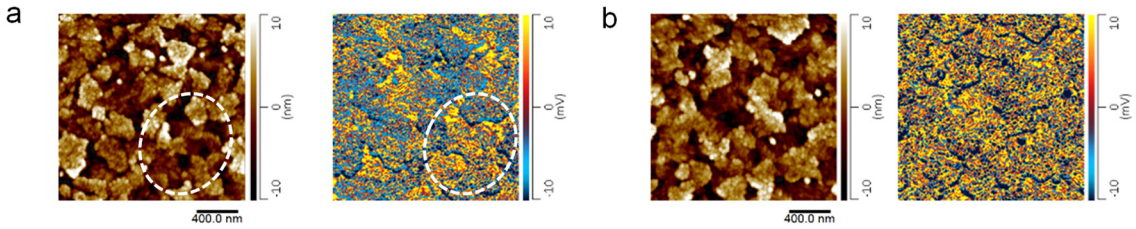

Supplementary Fig. 1. IR-AFM mapping of ITO/SAM substrates. (a) Spin-coated 2PACz. (b) Electrodeposited 2PACz.

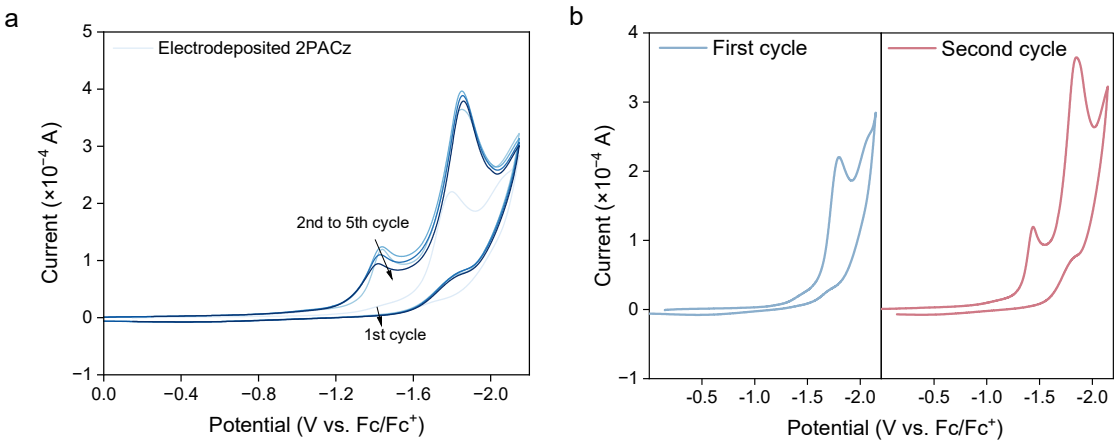

Supplementary Fig. 2. CVs during electrodeposition of 2PACz. (a) CVs from the 1st to 5th cycle; lighter traces denote earlier cycles. (b) A new feature near −1.4 V appears in the second scan but is absent in the first, consistent with the onset of an interfacial electrochemical process involving 2PACz and ITO during potential cycling.

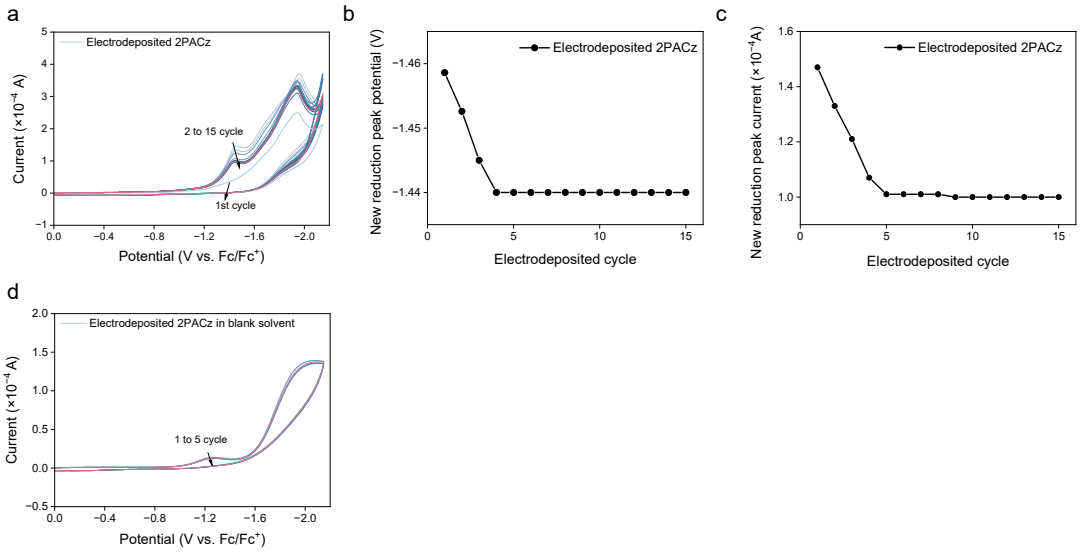

Supplementary Fig. 3. Evolution and reductive stability of electrodeposited 2PACz. (a) CVs during 2PACz electrodeposition over 15 cycles under reductive potentials. (b), (c) Evolution of the reduction feature near −1.4 V as a function of cycle number, showing pronounced changes during the first five cycles and a plateau thereafter, consistent with saturation of the electrodeposition process. (d) Reductive stability test of electrodeposited 2PACz in a blank electrolyte, showing negligible variation.

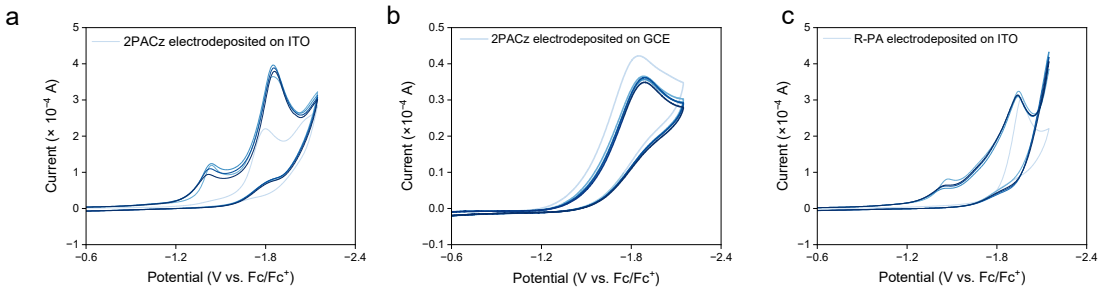

Supplementary Fig. 4. Assigning the near −1.4 V reduction peak to the phosphonic-acid–ITO interface by controlled CV comparisons. (a) 2PACz on ITO. A reduction peak appears at near −1.4 V. (b) 2PACz on glassy carbon electrode (GCE). The peak is absent under the same electrolyte and scan window. (c) 1-butanephosphonic acid (R-PA, phosphonic-acid control without carbazole) on ITO. The near −1.4 V peak reappears. Together, these comparisons show that the near −1.4 V feature is observed only when both the phosphonic-acid group and the ITO substrate are present, supporting its assignment to an interfacial electrochemical process involving the phosphonic-acid moiety and ITO.

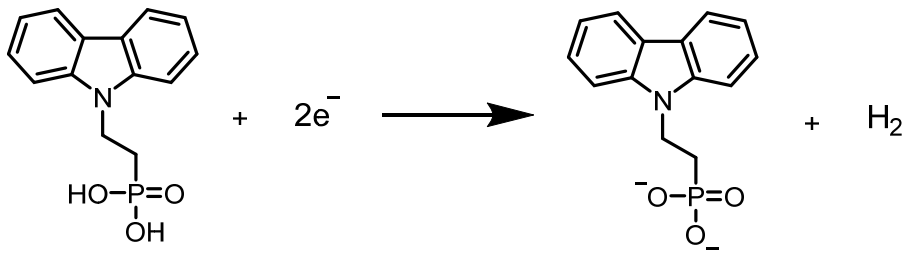

Supplementary Fig. 5. Cathodic polarization of 2PACz and the coupled hydrogen evolution process, supporting electrochemically promoted deprotonation of the phosphonic-acid group.

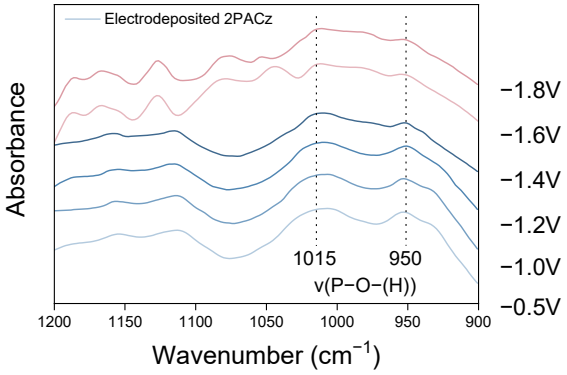

Supplementary Fig. 6. Operando electrochemical infrared spectroscopy of 2PACz under reductive polarization.

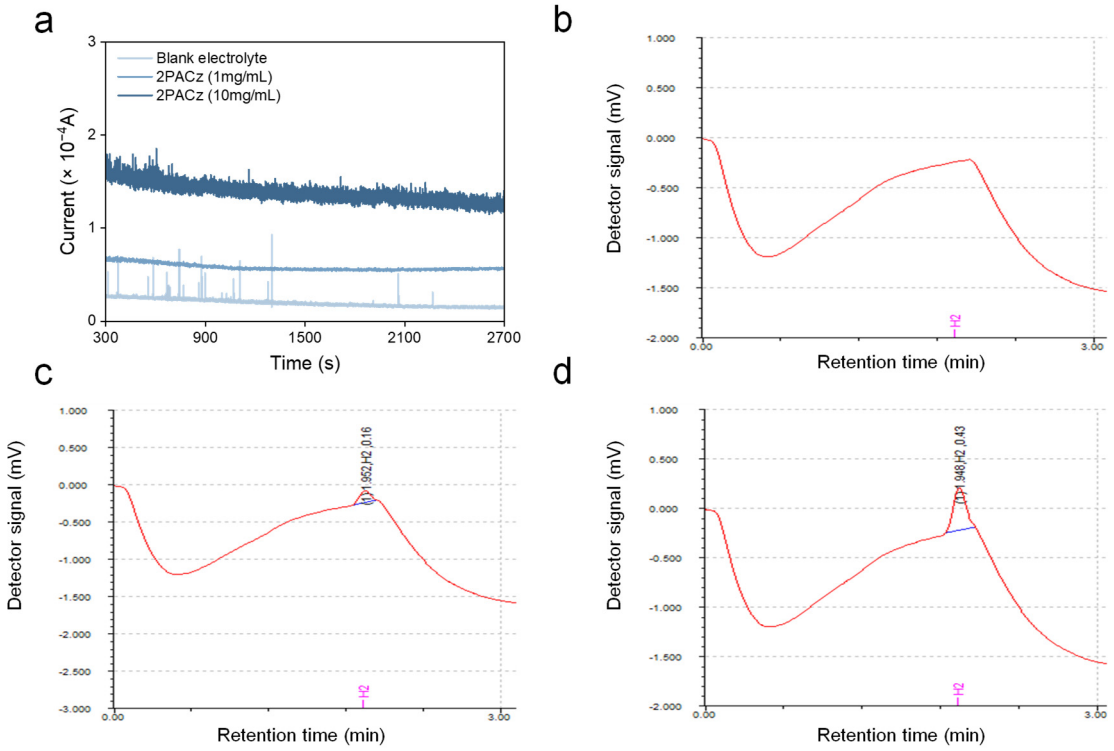

Supplementary Fig. 7. Controlled-potential electrolysis (−1.8 V vs Fc/Fc^{+}) of 2PACz in a sealed cell, with GC detection of evolved H_2 under cathodic polarization. (a) Current–time (I–t) traces recorded for blank electrolyte, 1 mg mL^{-1} 2PACz, and 10 mg mL^{-1} 2PACz under a constant reductive potential. (b) Gas chromatography (GC) traces of the headspace collected after electrolysis, showing negligible H_2 for the blank electrolyte. (c) Detectable H_2 for 1 mg mL^{-1} 2PACz. (d) Increased H_2 for 10 mg mL^{-1} 2PACz after the same electrolysis duration. These results support electrochemically promoted deprotonation of the phosphonic-acid group under reductive polarization.

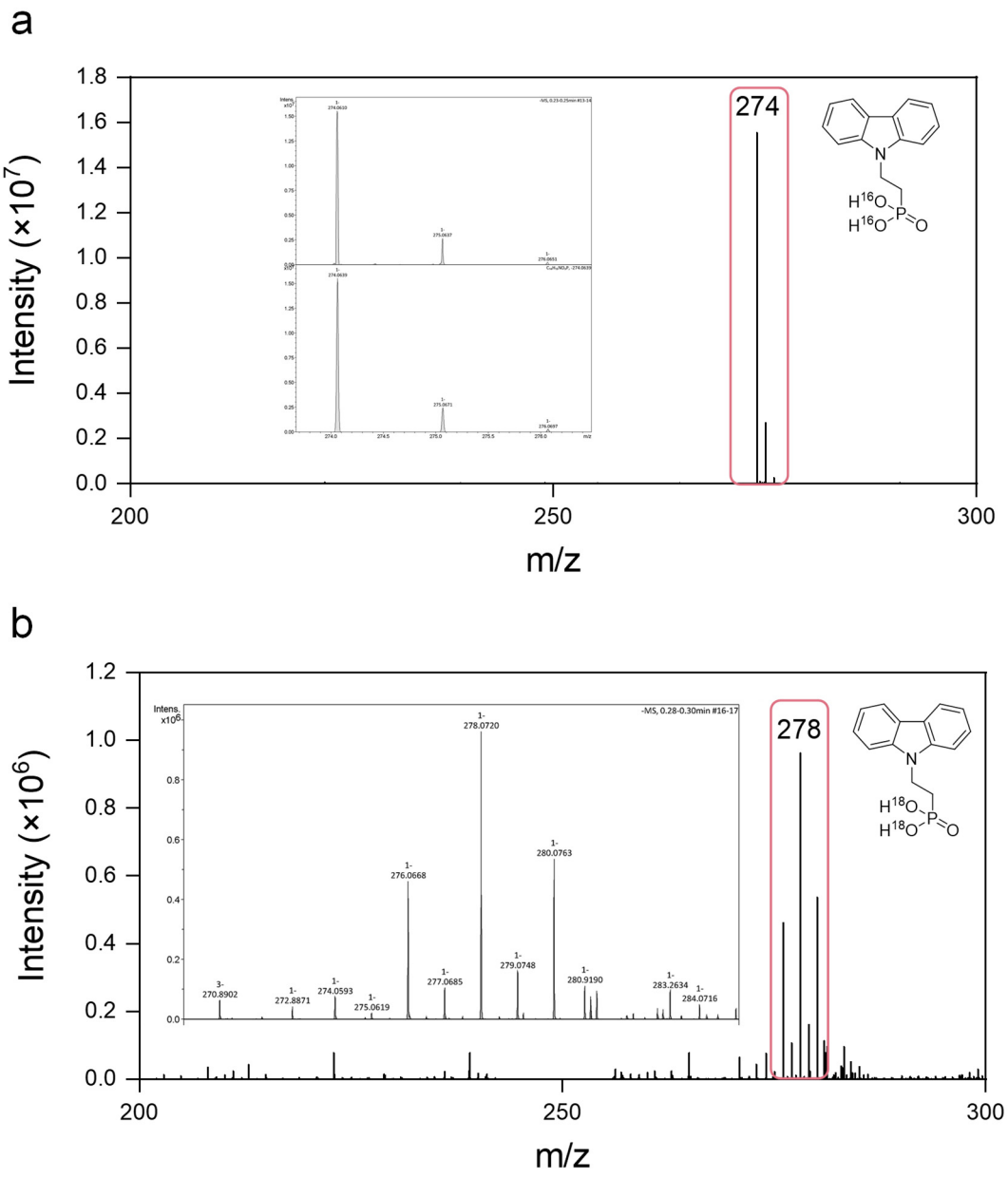

Supplementary Fig. 8. Mass spectrometric confirmation of ^{18}O labelling in 2PACz. (a) ^{16}O-2PACz. (b) ^{18}O-2PACz.

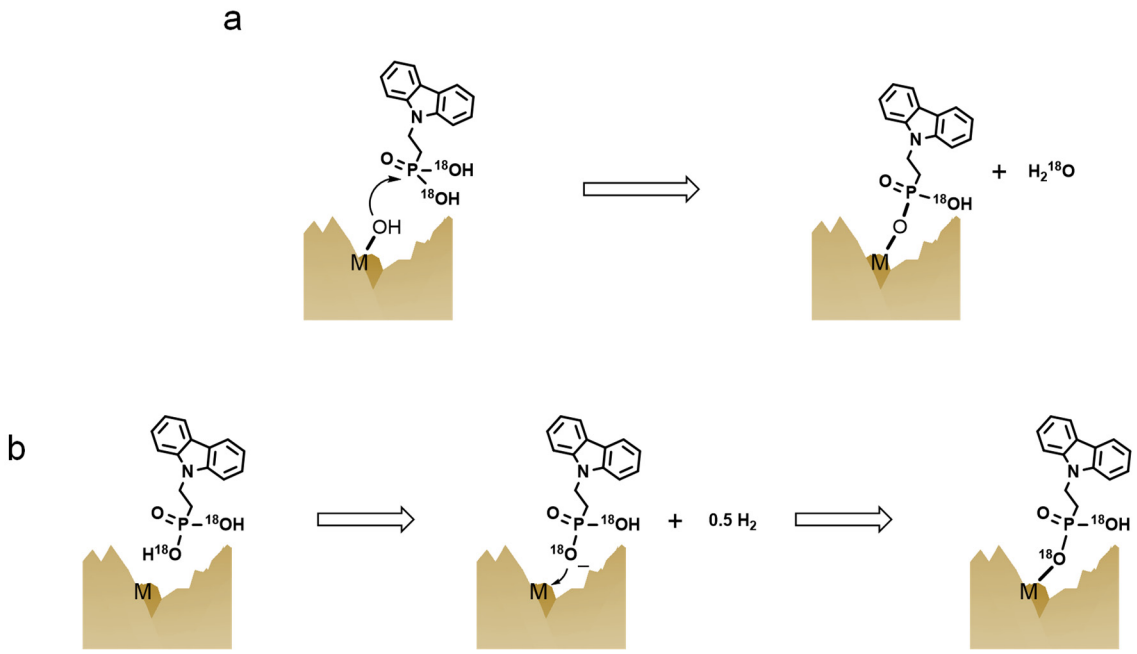

Supplementary Fig. 9. Representative anchoring pathways for P–O–M bond formation between 2PACz and ITO. (a) Dehydration condensation with surface M–OH groups. (b) Inner-sphere binding of deprotonated phosphonate (P–O^{-}) at In and Sn surface sites on ITO.

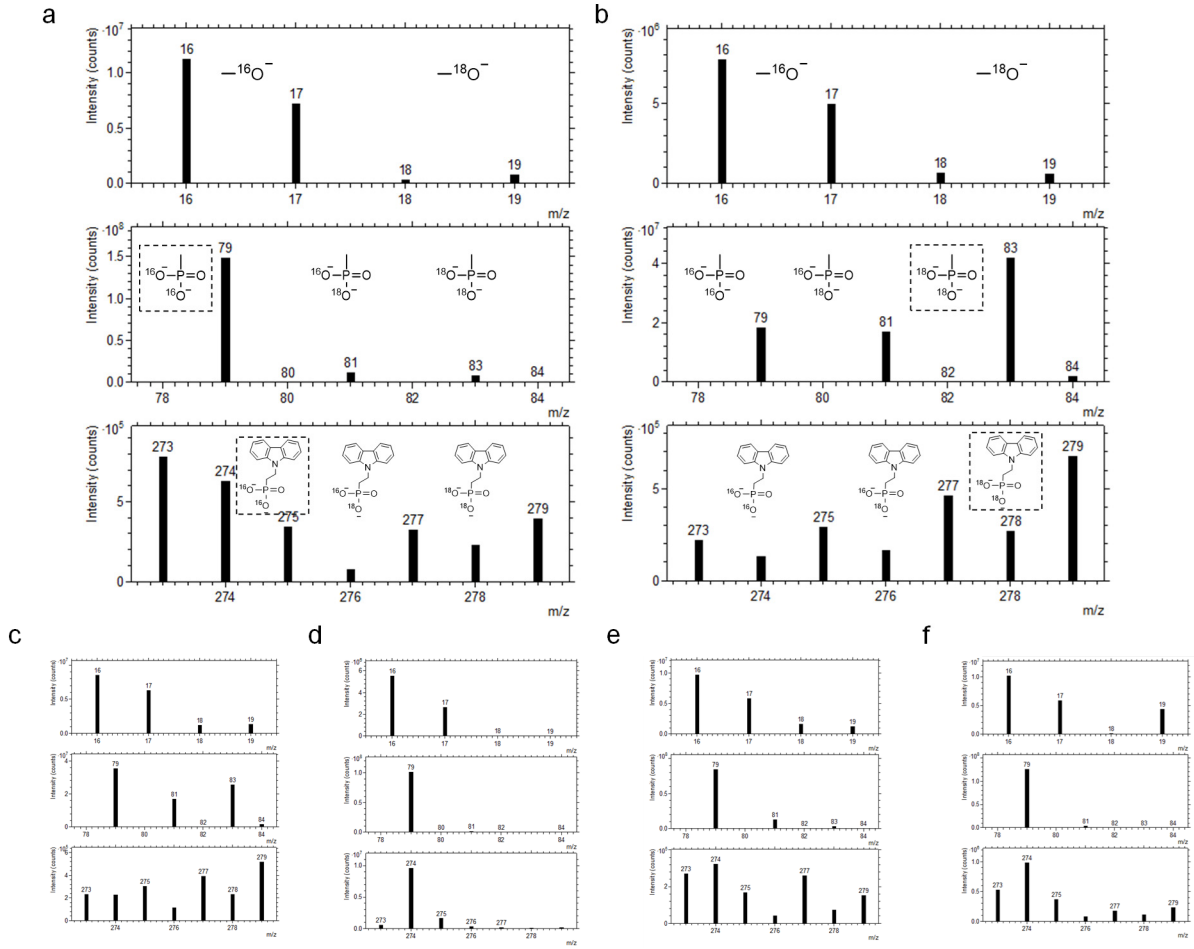

Supplementary Fig. 10. ToF–SIMS isotope tracing of interfacial 2PACz species on ITO under spin-coating and electrodeposition. (a) Spin-coated ^{18}O-2PACz on $^{16}O_2$-plasma-treated ITO. (b) Electrodeposited ^{18}O-2PACz on ITO without plasma. (c) Electrodeposited ^{18}O-2PACz on $^{16}O_2$-plasma-treated ITO. (d) Spin-coated ^{16}O-2PACz on $^{16}O_2$-plasma-treated ITO. (e) Spin-coated ^{16}O-2PACz on $^{18}O_2$-plasma-treated ITO. (f) Electrodeposited ^{16}O-2PACz on $^{18}O_2$-plasma-treated ITO. All samples were rinsed with DMF after film formation to remove non-anchored 2PACz. The isotope patterns were used to compare the relative contributions of substrate-derived oxygen incorporation and molecule-derived oxygen retention, rather than to assign a fully binary anchoring mechanism.

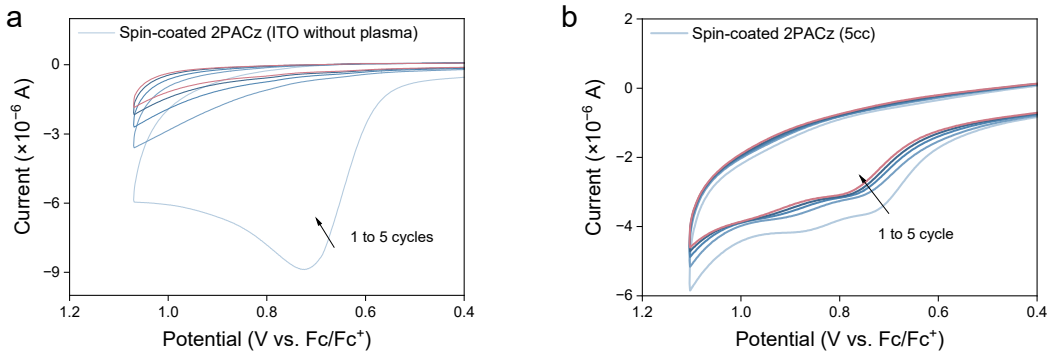

Supplementary Fig. 11. Desorption behavior of 2PACz prepared under different conditions, probed by blank-electrolyte CV. (a) Spin-coated 2PACz on ITO without O_2-plasma pretreatment shows a pronounced scan-to-scan reduction of the carbazole peak (near 0.8 V) in a blank-electrolyte solution, consistent with weaker anchoring. (b) A higher-concentration spin-coated 2PACz film exhibits an even larger decay, indicative of increased physisorbed coverage. Together, these controls suggest that the species removed during blank-electrolyte CV are dominated by physisorbed 2PACz rather than the chemisorbed molecules.

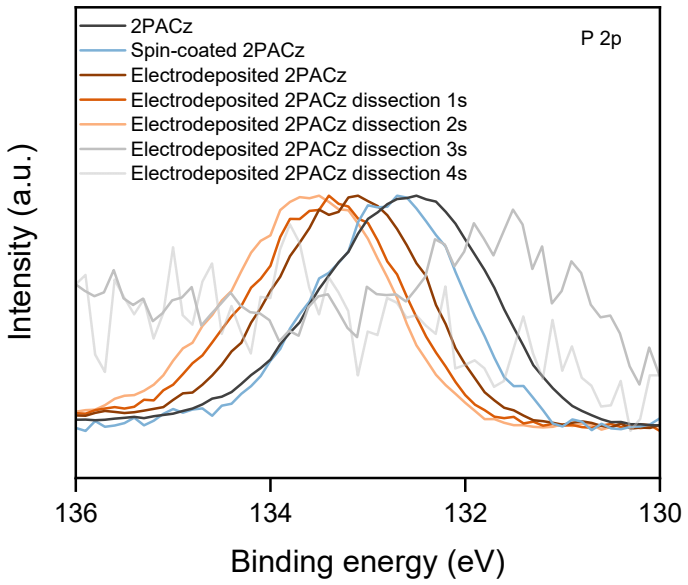

Supplementary Fig. 12. Reference P 2p XPS for peak assignment and anchoring identification. Pristine 2PACz shows a P 2p signal dominated by the P–O–H component of the phosphonic acid group. Spin-coated 2PACz on ITO exhibits a slightly higher P 2p binding energy, indicative of interaction with the ITO substrate. In depth-profiled electrodeposited 2PACz, the bottommost interface (2s etch) is selected as representative of direct anchoring to ITO, resolving the characteristic P–O–M component. These reference spectra underpin the deconvolution used in the main text, where P–O–H is assigned from pristine 2PACz and P–O–M from the interfacial slice of electrodeposited 2PACz, consistent with P–O–M anchoring at the SAM–ITO interface.

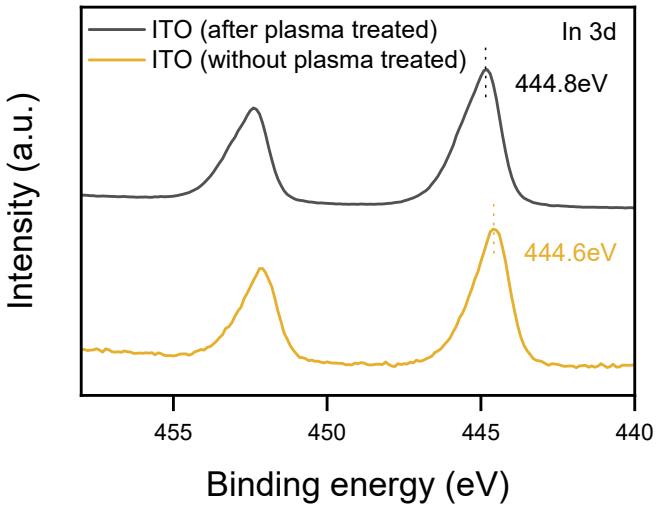

Supplementary Fig. 13. In 3d XPS controls isolate plasma-induced shifts. Blank ITO without plasma treatment is compared with plasma-treated ITO; the plasma-treated surface shows a clear binding-energy shift in the In 3d core level, consistent with plasma-induced surface modification.

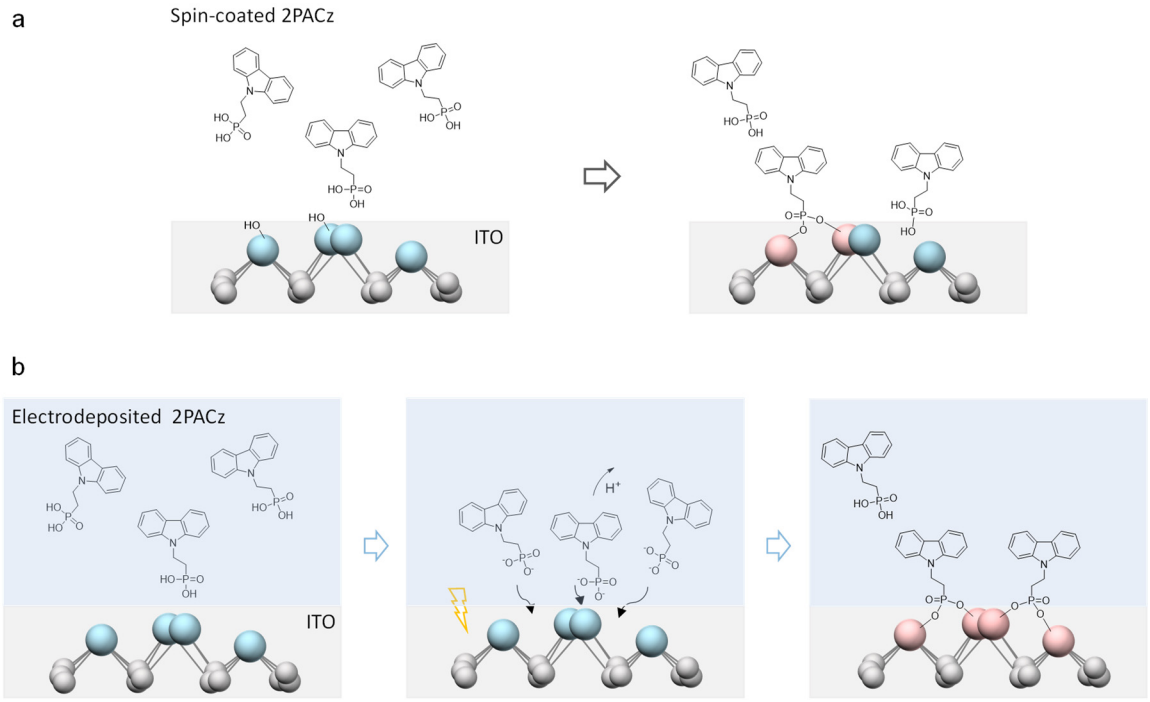

Supplementary Fig. 14. Schematic comparison of representative anchoring scenarios on ITO. (a) Spin-coated 2PACz anchoring is strongly affected by surface M–OH groups, which can react with phosphonic-acid groups through dehydration condensation to form P–O–M linkages. (b) Electrodeposited 2PACz was prepared without plasma pretreatment under the standard protocol. Under reductive potentials, deprotonated phosphonate species provide a less hydroxyl-dependent pathway for forming P–O–M interactions with accessible In and Sn surface sites. These two pathways may coexist, with their relative contributions depending on the deposition route and surface condition.

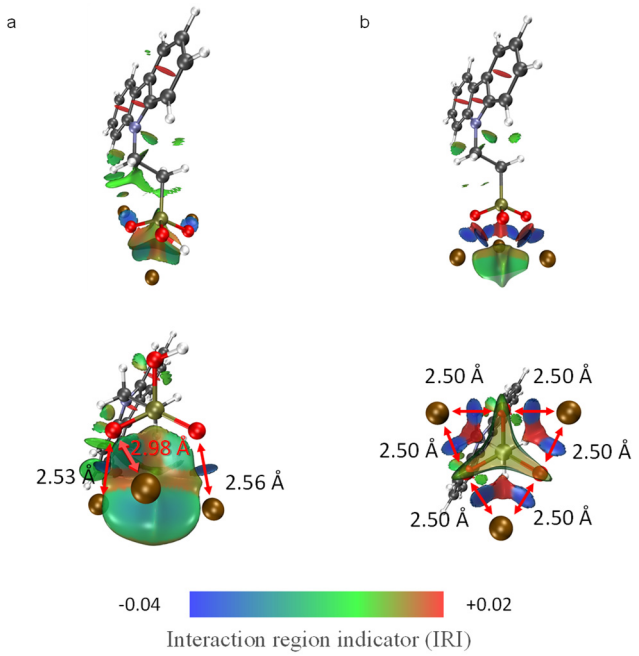

Supplementary Fig. 15. DFT comparison of interfacial anchoring for spin-coated versus electrodeposited 2PACz on ITO. (a) Spin-coated 2PACz. (b) Electrodeposited 2PACz. DFT-optimized structures show shorter P–O–In distances for the deprotonated phosphonate binding model, consistent with enhanced interfacial interaction under electrodeposition.

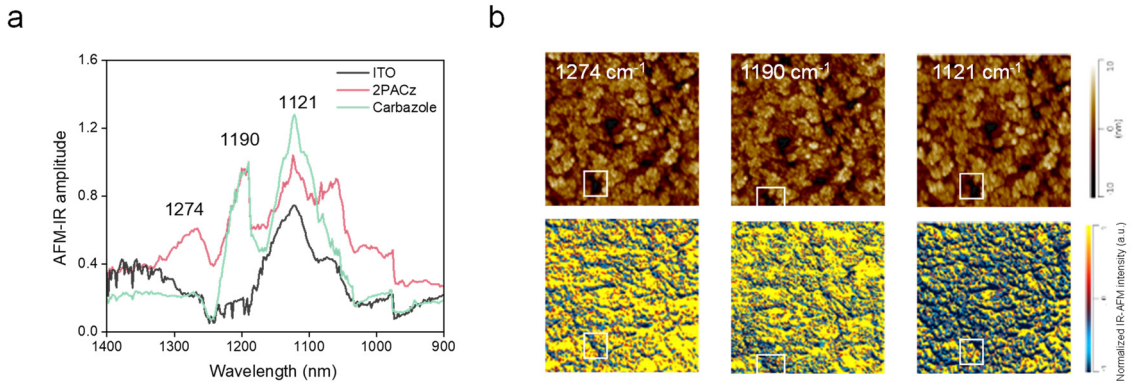

Supplementary Fig. 16. Reference infrared spectra and multi-band IR-AFM mapping for peak assignment and spatial verification. (a) Infrared spectra used for peak assignment (bare ITO, 2PACz, and carbazole). (b) IR-AFM amplitude maps acquired at selected wavenumbers to visualize the spatial distribution. Based on these controls and previous literature, we assign the band at ~1274 cm^{-1} to vibrations of the phosphonate headgroup. The feature at ~1190 cm^{-1} is attributed to a carbazole aromatic-ring-related vibration, whereas the band at ~1121 cm^{-1} originates from the substrate response.

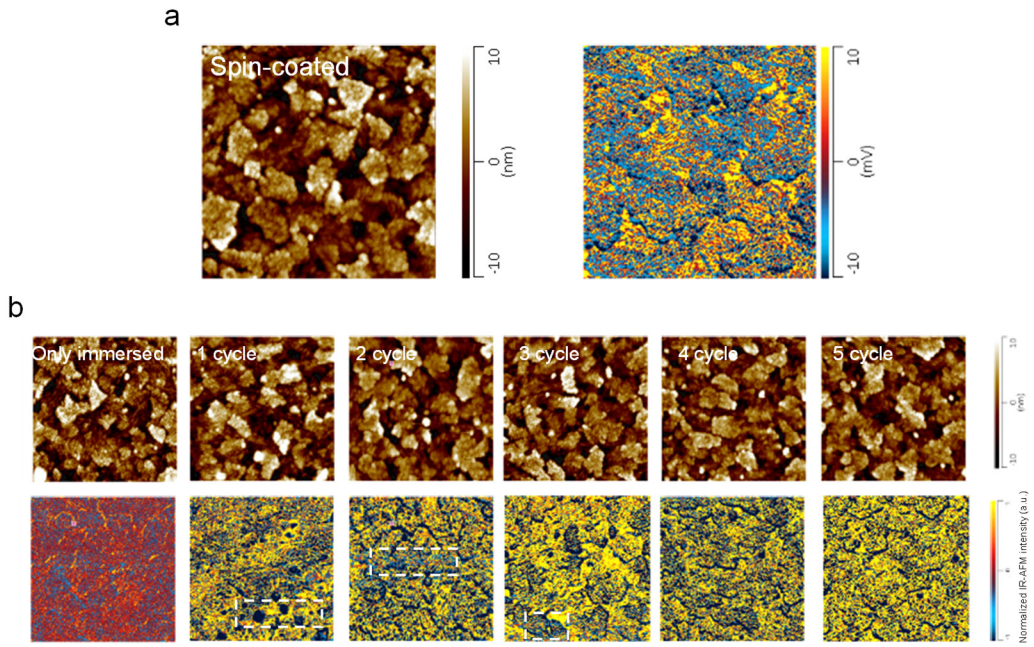

Supplementary Fig. 17. IR-AFM mapping of 2PACz prepared by different methods. (a) ITO/spin-coated 2PACz. (b) ITO/electrodeposited 2PACz as a function of cycle number. AFM height and IR-AFM absorption at 1274 cm^{-1} reveal patchy coverage with preferential accumulation in ITO recesses for spin-coated 2PACz. In the electrodeposited series, 1–3 cycles exhibited pronounced uncovered regions (blue/black regions with low 2PACz-related signal), indicating discontinuous SAM coverage on the ITO surface. From 4 cycles onward, these uncovered regions largely disappeared, consistent with potential-driven molecular rearrangement and re-anchoring during electrodeposition.

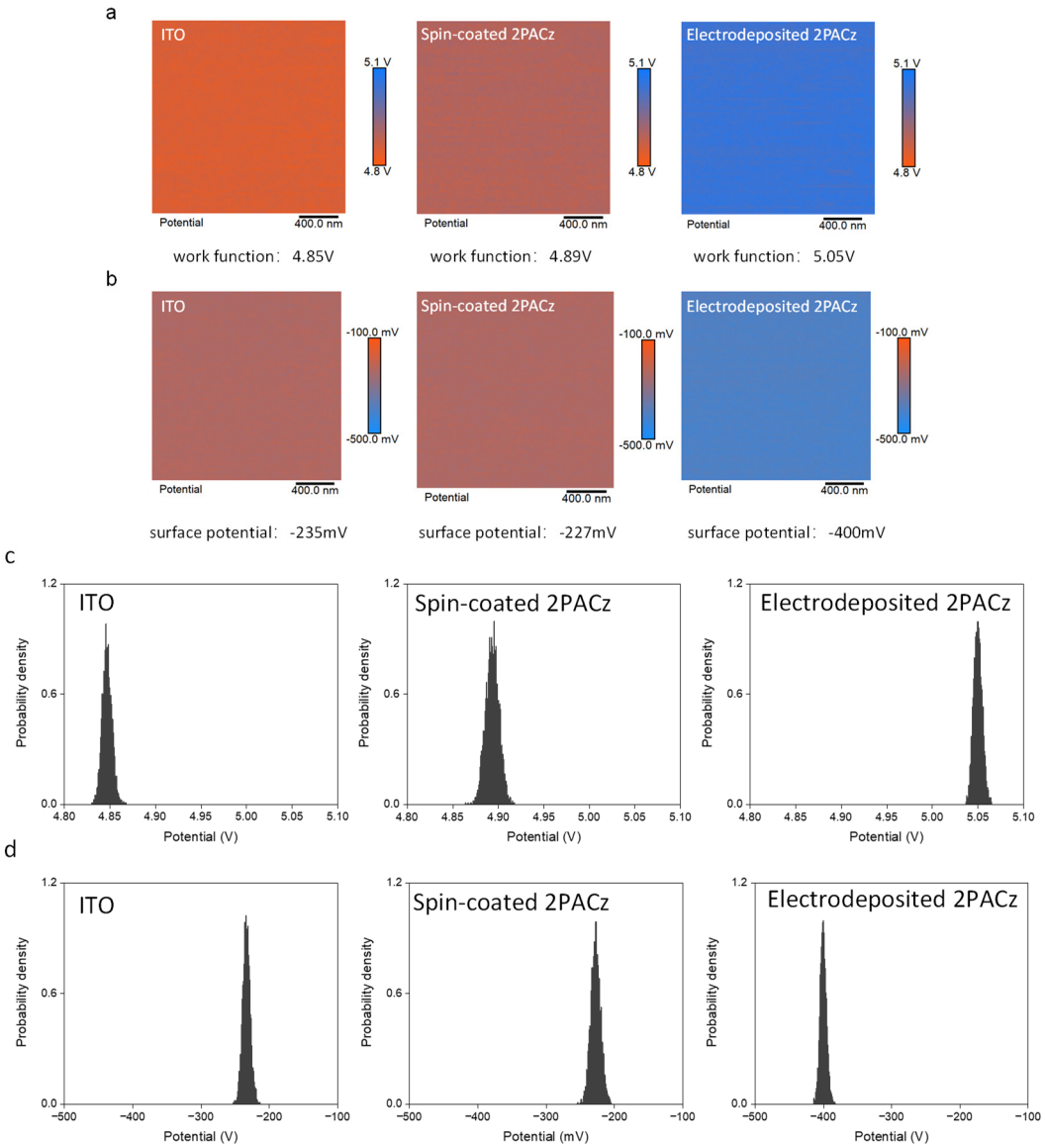

Supplementary Fig. 18. Work function (KPFM) and surface-potential distributions of ITO and SAM-modified contacts. (a) KPFM contact potential difference (CPD) maps and area-averaged work function obtained via $\Phi_{samp} = \Phi_{tip} - q \cdot CPD$ for bare ITO, ITO/spin-coated 2PACz, and ITO/electrodeposited 2PACz. (b) Surface potential of spin-coated and electrodeposited 2PACz on ITO. (c) Work function distributions extracted from the maps in (a). (d) Surface potential distributions extracted from the maps in (b).

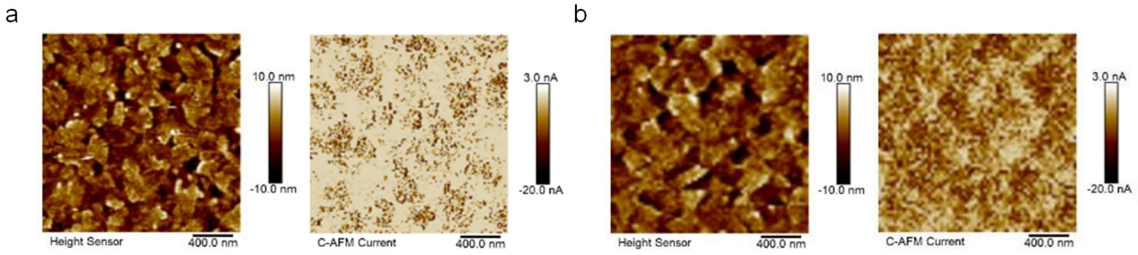

Supplementary Fig. 19. c-AFM current maps of SAMs prepared by different methods. (a) ITO/spin-coated 2PACz. (b) ITO/electrodeposited 2PACz. For spin-coated 2PACz, c-AFM maps show localized, spot-like conduction co-located with elevated ITO features, consistent with preferential accumulation in surface recesses and relatively sparse coverage on protrusions. The electrodeposited film shows uniform current extraction with weak dependence on the underlying topography. Overall, electrodeposited SAMs provide spatially uniform transport with reduced coupling to substrate roughness compared with spin-coated films.

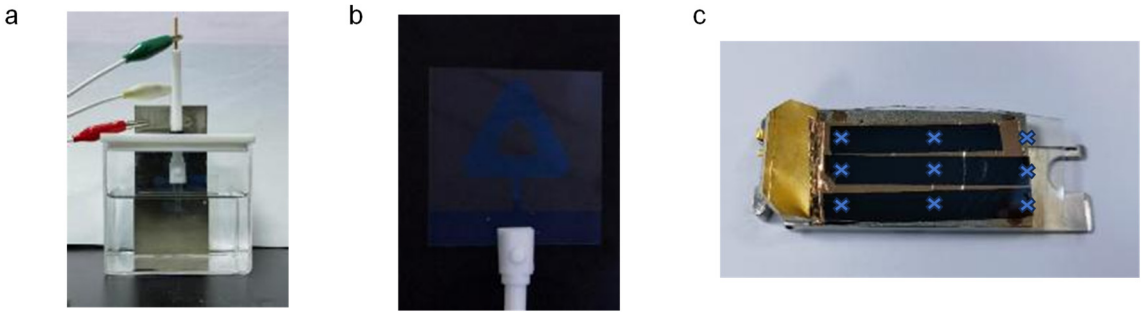

Supplementary Fig. 20. Electrodeposition of SAMs on large-area ITO substrates. (a) Schematic illustration of the electrodeposition setup for SAM fabrication on ITO substrates. (b) Photograph of an electrodeposited SAM on a 5 × 5 cm^2 patterned ITO substrate. (c) Uniformity evaluation of the electrodeposited SAM film by X-ray photoelectron spectroscopy (XPS); measurements were taken at nine randomly selected spots on an electrodeposited 10 × 10 cm^2 ITO substrate and show consistent film quality and uniform coverage across the large area.

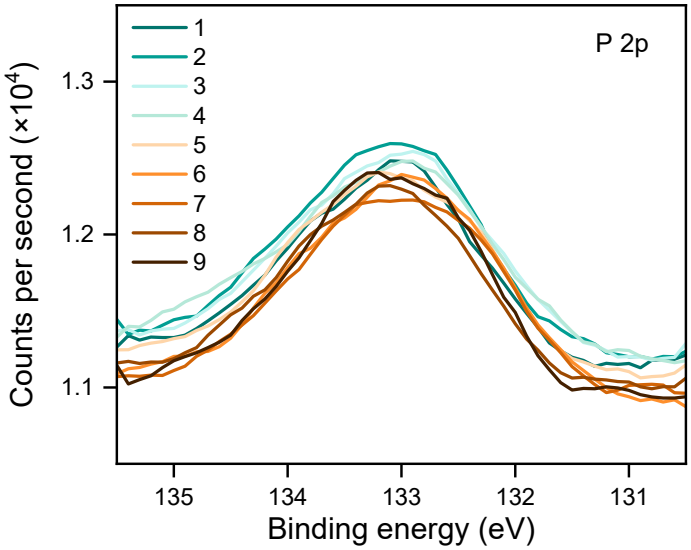

Supplementary Fig. 21. XPS P 2p mapping across a 10 × 10 cm^2 electrodeposited ITO/SAM substrate. Spectra from nine randomly selected locations show uniform SAM coverage over the large area, demonstrating the scalability and consistency of the electrodeposition process.

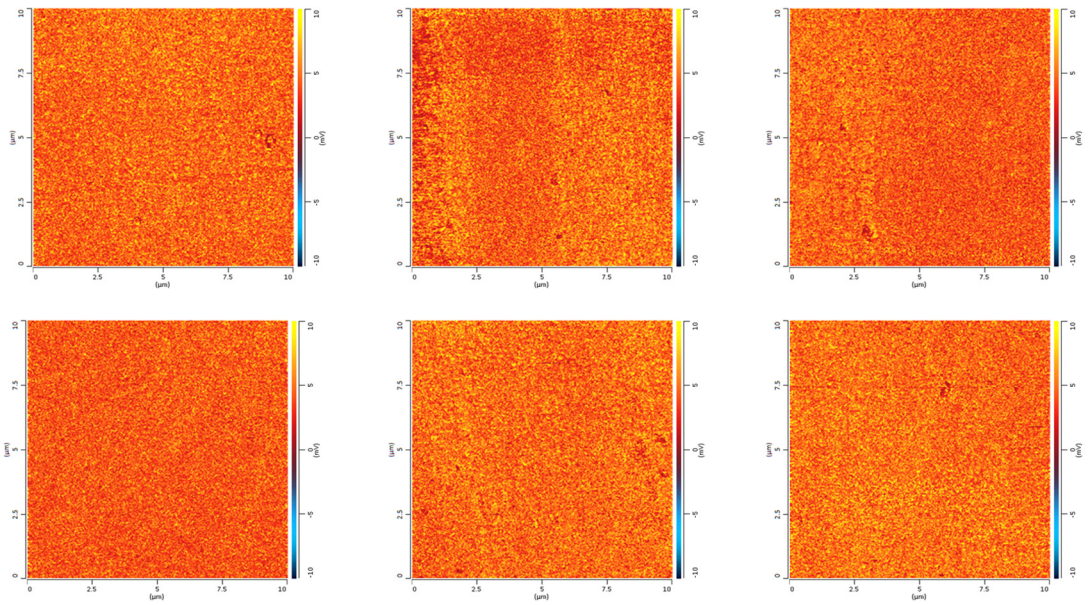

Supplementary Fig. 22. IR-AFM mapping across a 10 × 10 cm^2 electrodeposited ITO/SAM substrate. Images from six randomly selected locations show highly uniform SAM distribution across the large area, demonstrating that electrodeposition yields homogeneous coverage at scale.

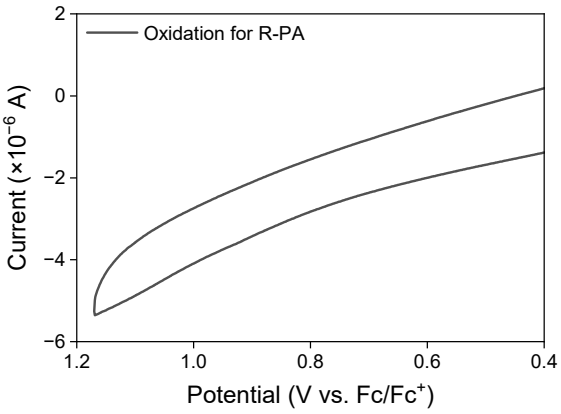

Supplementary Fig. 23. Electrochemical inertness of the phosphonic-acid anchoring group within the oxidative-coupling window. A cyclic voltammogram of hexylphosphonic acid (R–PA) on ITO in a non-aqueous $TBAPF_6$ electrolyte was recorded over 0–1.1 V. The trace shows no Faradaic features, indicating that the phosphonic-acid group is electrochemically inert throughout this range. This control supports that the oxidative-coupling step functionalizes the carbazole-facing side while preserving the phosphonate anchoring chemistry.

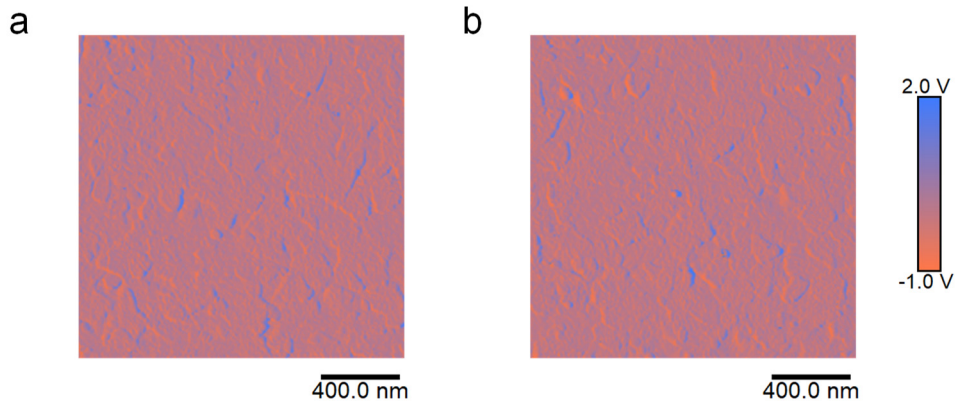

Supplementary Fig. 24. AFM phase mapping of ITO/electrodeposited 2PACz before and after exposure to the oxidative-coupling potential window. (a) Tapping-mode AFM phase image of ITO/electrodeposited 2PACz. (b) Phase image after cycling an identically prepared substrate in a blank $TBAPF_6$ electrolyte (0–1.1 V). This result supports that the second electrochemical step preserves the electrodeposited base layer while enabling subsequent functionalization.

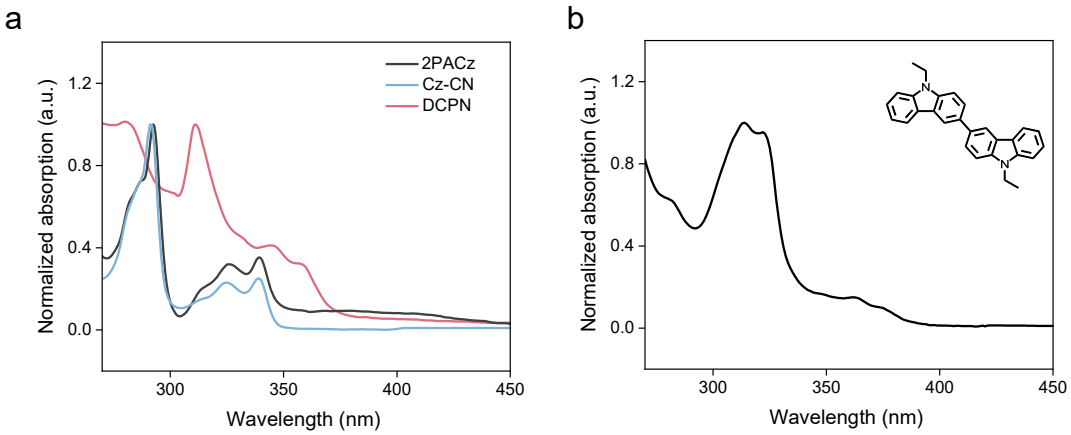

Supplementary Fig. 25. UV–vis absorption fingerprints of electrochemically coupled DCPN. (a) Spectra of 2PACz, Cz–CN, and DCPN. (b) Spectrum of a bicarbazole reference. In DCPN, the monomeric carbazole band is strongly attenuated and a new band appears at 310 nm. The band position and lineshape match the bicarbazole reference, consistent with carbazole–carbazole coupling during electrochemical oxidative coupling.

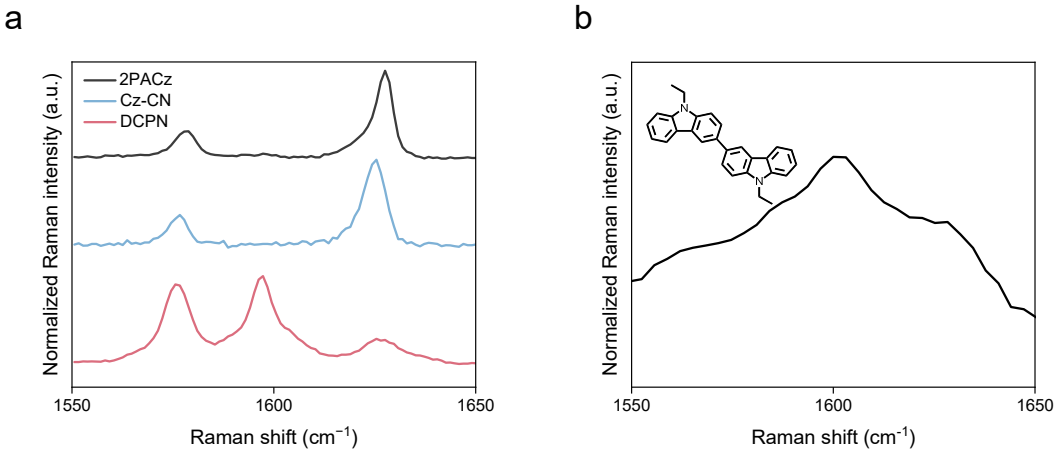

Supplementary Fig. 26. Raman fingerprints of carbazole–carbazole coupling in DCPN (532 nm excitation). (a) Spectra of 2PACz, Cz–CN, and DCPN. (b) Spectrum of a bicarbazole reference. In DCPN, monomeric carbazole modes are strongly attenuated and a new band appears near 1600 cm^{-1}. The band position and lineshape match the bicarbazole reference, consistent with carbazole–carbazole coupling during electrochemical oxidative coupling.

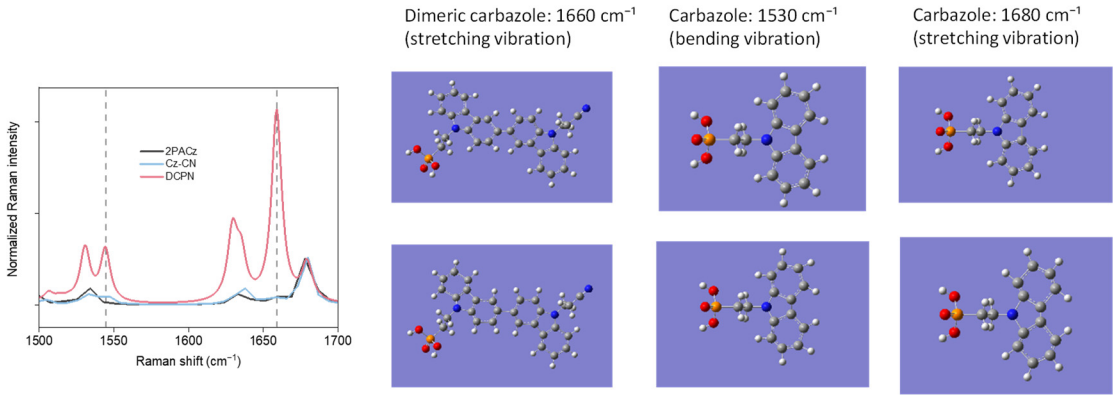

Supplementary Fig. 27. Density functional theory (DFT) calculated Raman spectra of 2PACz, Cz–CN, and DCPN. Dimeric carbazole exhibits an additional stretching mode relative to the monomer, yielding an extra peak consistent with the experimental Raman spectra.

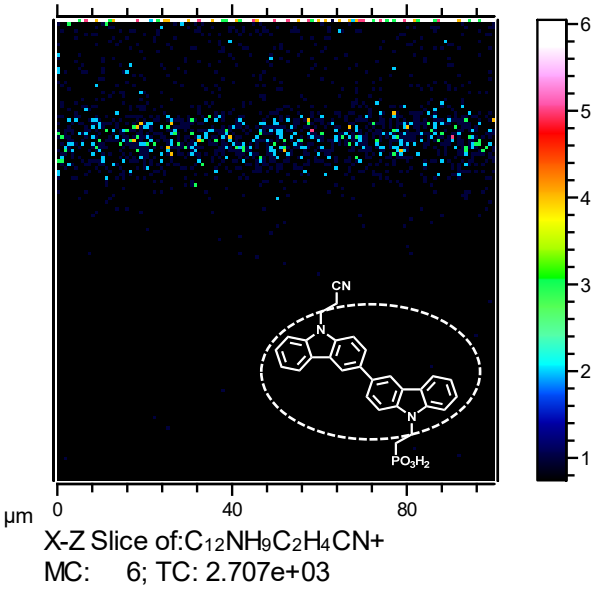

Supplementary Fig. 28. Cross-sectional ToF–SIMS mapping of DCPN fragments in the perovskite stack: X–Z positive-ion image of the diagnostic carbazole–carbazole fragment from DCPN ($C_{12}NH_9C_2H_4CN^+$). The signal localizes to the SAM layer, evidencing dimeric carbazole within the molecular layer. Detection of this dimer-derived fragment corroborates on-surface oxidative coupling to form DCPN.

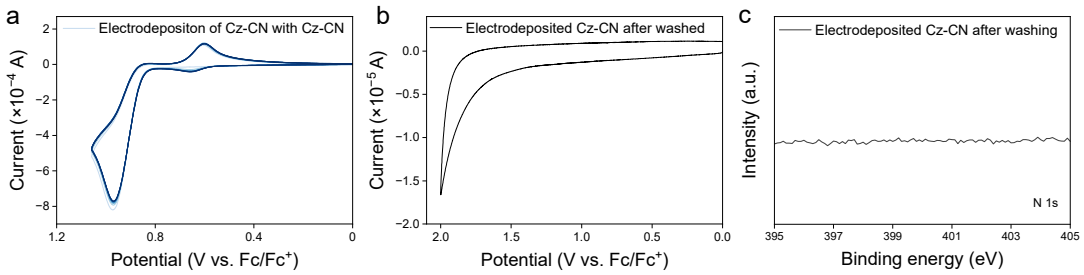

Supplementary Fig. 29. CV and XPS evidence for Cz–CN homocoupling and its removal by acetonitrile rinse. (a) ITO was immersed in a Cz–CN (1 mg mL^{-1}) electrolyte and scanned over 0–1.05 V; the trace shows two features: the carbazole oxidation wave and a second wave attributed to bicarbazole formed via Cz–CN homocoupling. (b) After an ACN rinse and transfer to a blank electrolyte, both features are absent on the above-prepared substrate, indicating that the species are not covalently anchored and are removed by rinsing. (c) Post-rinse XPS N 1s spectra show nitrogen features associated with Cz (monomer) and Cz–Cz (dimer) reduced to baseline, consistent with complete removal of unbound species. Together, these results indicate that Cz–CN homocoupled species do not persist within the electrodeposited DCPN layer.

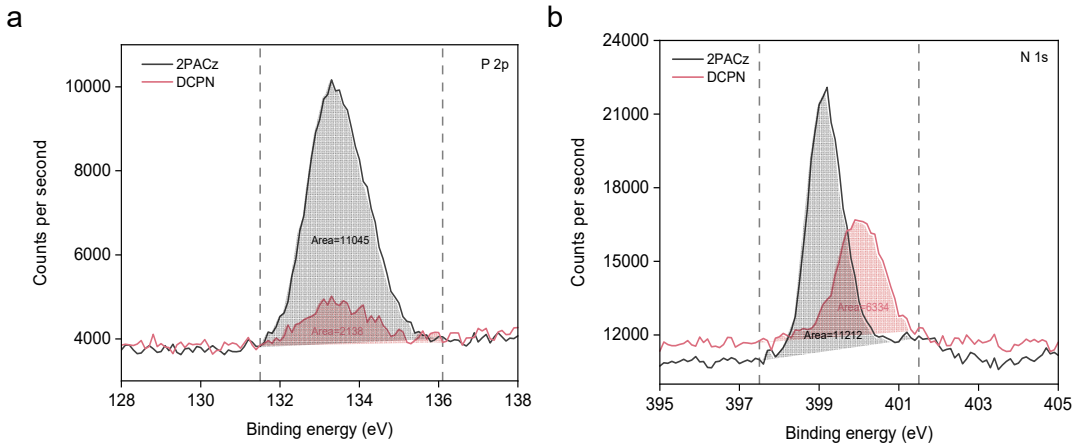

Supplementary Fig. 30. XPS stoichiometry of 2PACz and DCPN SAMs. (a) P 2p region. (b) N 1s region. For the coupled film DCPN, we obtain N/P = 2.96, whereas 2PACz gives N/P = 1.0. Because 2PACz carries $N/P = 1$ and DCPN carries $N/P = 3$, the coupling fraction f follows $N/P = 1 + 2f$, substituting $f = (2.96 - 1)/2 = 0.98$ (98% conversion). This value provides a semi-quantitative estimate of the coupling fraction. Together with ToF-SIMS identification and spectral fingerprints (UV–vis, Raman), this stoichiometric analysis substantiates quantitative on-surface coupling.

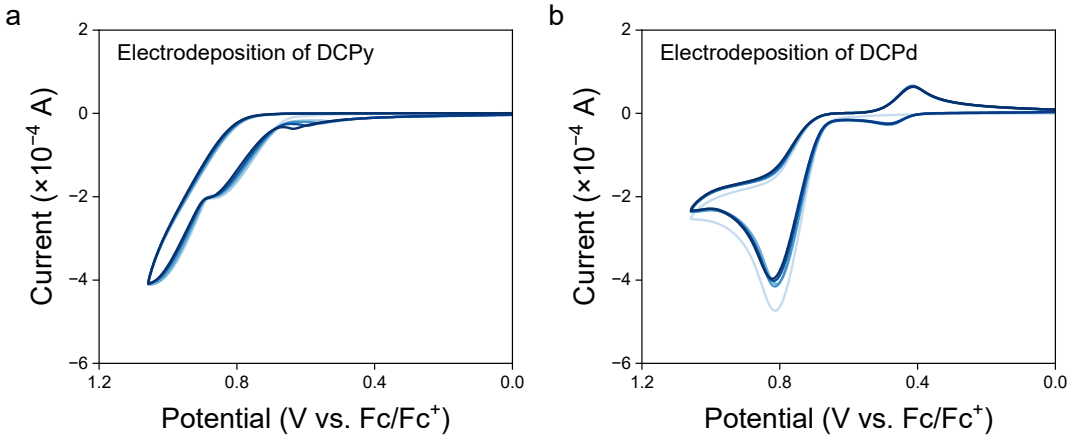

Supplementary Fig. 31. Cyclic voltammograms used for electrodeposition of DCPy and DCPd. (a) DCPy. (b) DCPd.

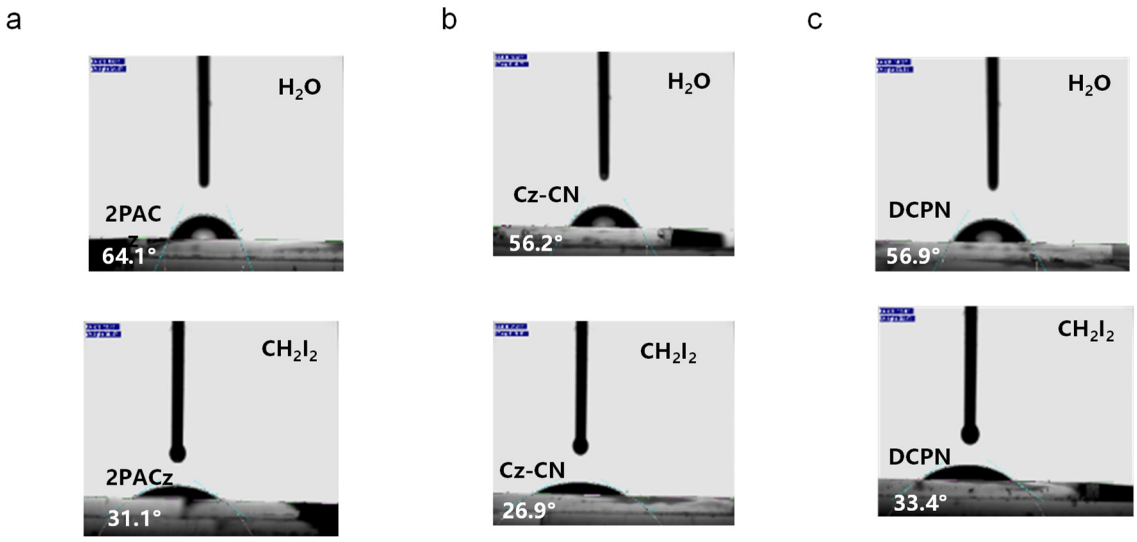

Supplementary Fig. 32. Contact-angle measurements of deposited SAM films. (a) 2PACz. (b) Cz–CN. (c) DCPN.

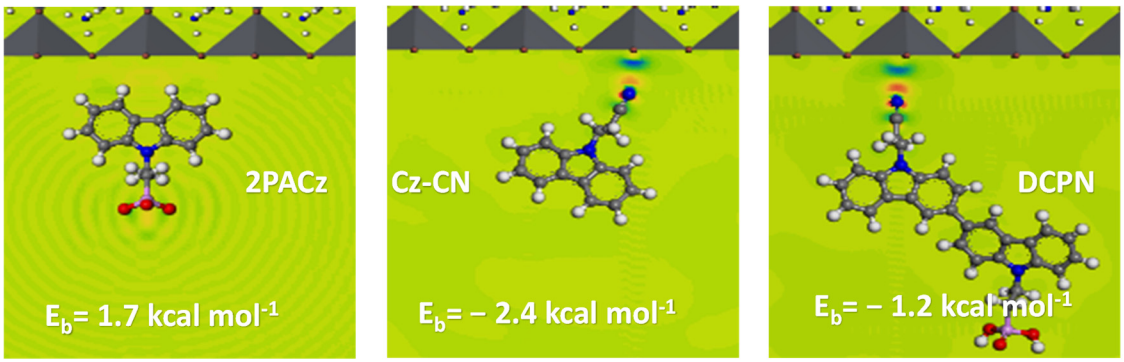

Supplementary Fig. 33. Electron-density–difference (EDD) maps at the perovskite–SAM interface. (a) 2PACz. (b) Cz–CN. (c) DCPN. For each perovskite–SAM pair, the EDD and binding energy (E_b) are evaluated. Relative to 2PACz, DCPN shows more pronounced interfacial charge redistribution and a more negative E_b, indicating enhanced interfacial affinity while preserving the phosphonate-anchor/nitrile-terminus motif.

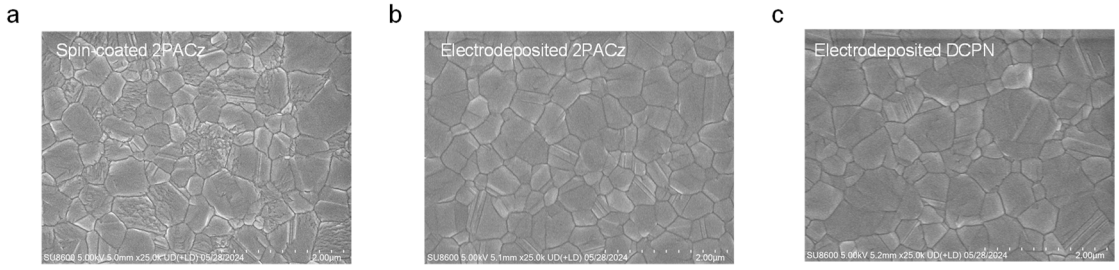

Supplementary Fig. 34. SEM of the top perovskite interface on different SAMs. (a) Spin-coated 2PACz. (b) Electrodeposited 2PACz. (c) Electrodeposited DCPN.

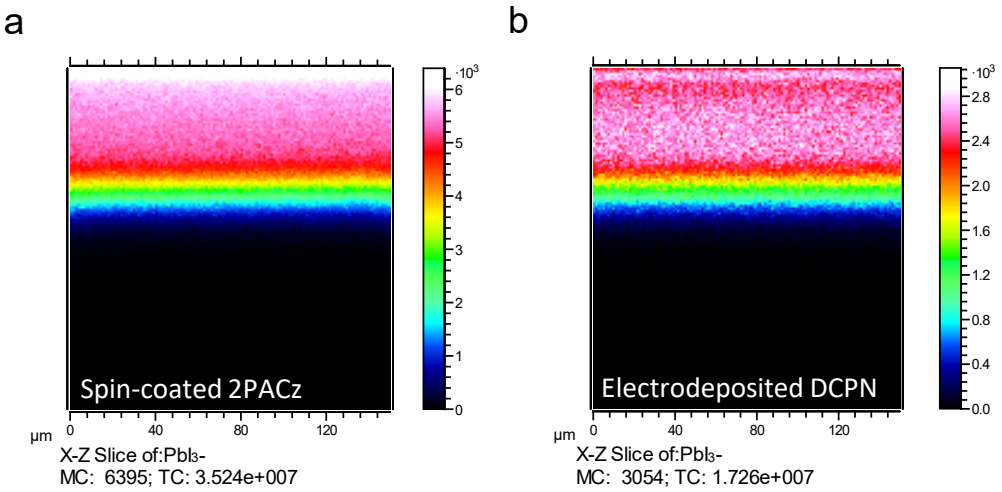

Supplementary Fig. 35. ToF–SIMS X–Z slices of the PbI_3^- signal for perovskite films on different SAMs. (a) Spin-coated 2PACz. (b) Electrodeposited DCPN. The 2PACz sample shows a high-intensity interfacial band indicative of PbI_2 enrichment, whereas the DCPN sample shows a smooth depth profile without an interfacial spike, consistent with a more uniform vertical distribution of PbI_2.

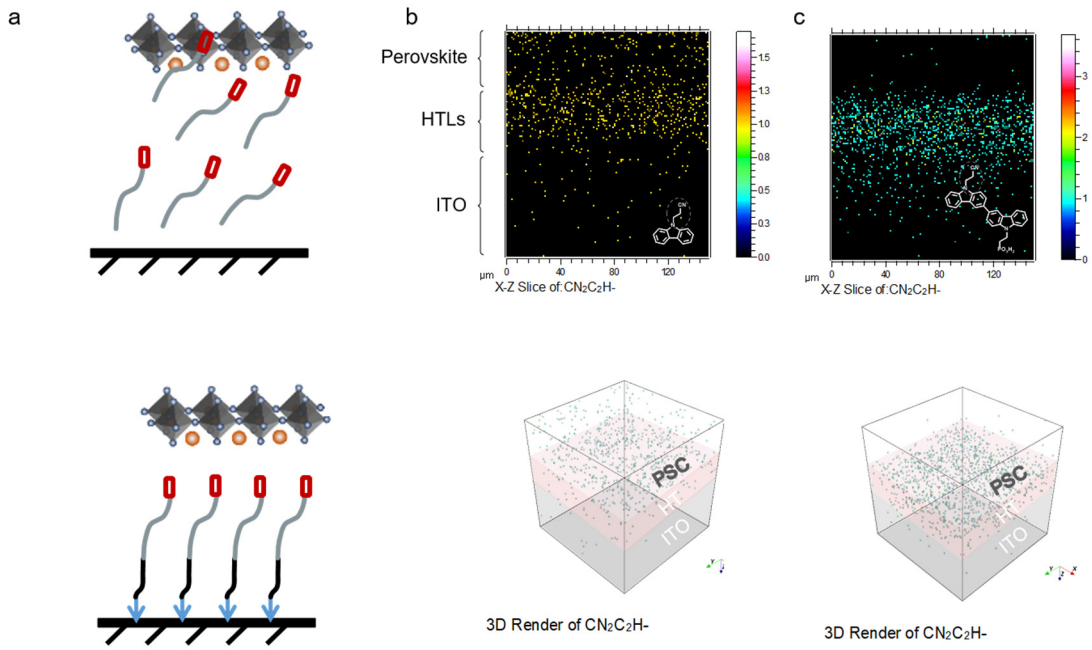

Supplementary Fig. 36. Interfacial fate of spin-coated Cz–CN versus electrodeposited DCPN. (a) Schematic highlighting interfacial differences when Cz–CN or DCPN serves as the interface layer in PSCs. (b) ToF–SIMS vertical distribution of Cz–CN after perovskite deposition on ITO/spin-coated Cz–CN; the nitrile-terminated molecules show upward diffusion into the perovskite, consistent with surface affinity and loss of interfacial continuity. (c) ToF–SIMS vertical distribution of DCPN after perovskite deposition on ITO/electrodeposited DCPN; the phosphonate anchor immobilizes the carbazole dimer at the oxide, and the DCPN-derived signal remains confined to the buried interface during perovskite processing. Overall, electrodeposited DCPN suppresses upward migration and preserves an abrupt buried interface suitable for device fabrication.

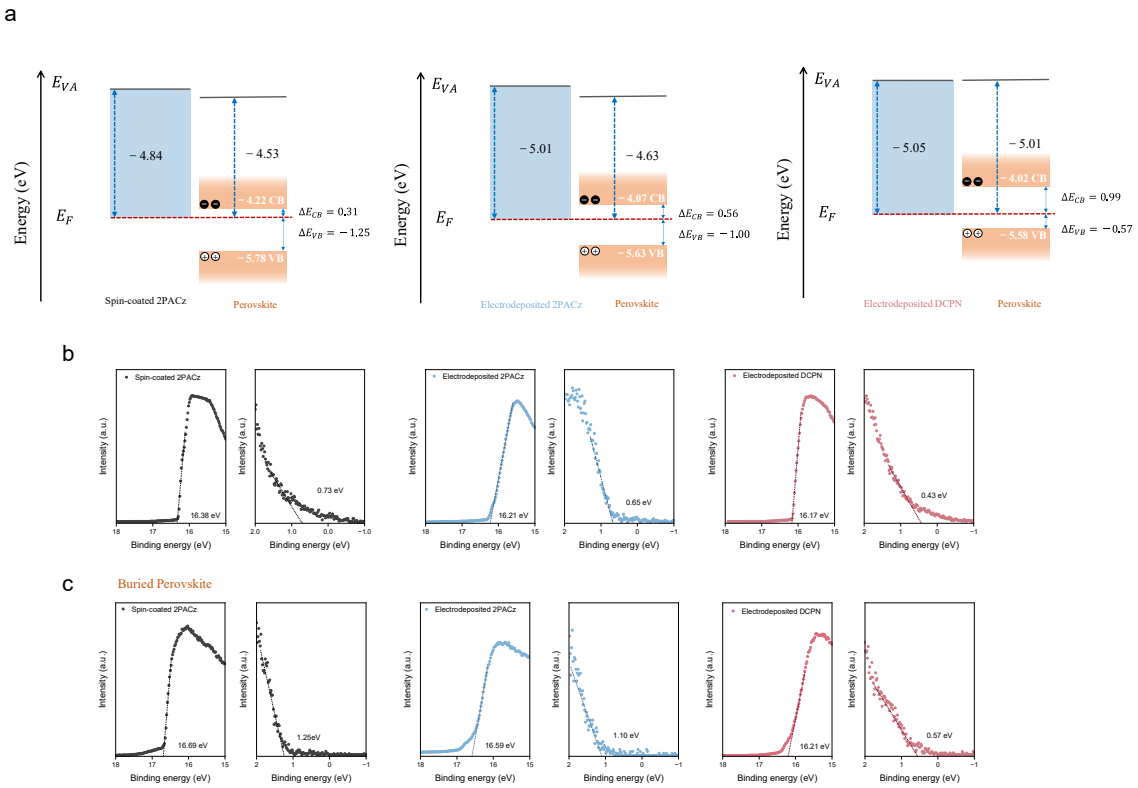

Supplementary Fig. 37. UPS analysis of energy-level alignment in SAMs and buried perovskite interfaces. (a) Schematic energy-level alignment diagrams constructed from the UPS results for devices based on different SAMs. (b) UPS spectra of the corresponding SAM-modified ITO substrates. (c) UPS spectra of the buried perovskite interfaces formed on the different SAMs.

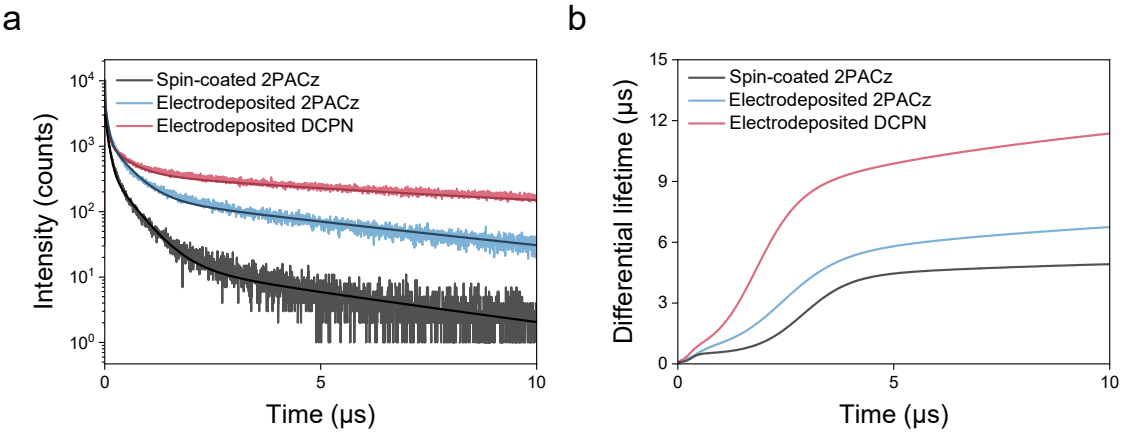

Supplementary Fig. 38. TRPL fitting and differential-lifetime analysis of SAM/perovskite half stacks.

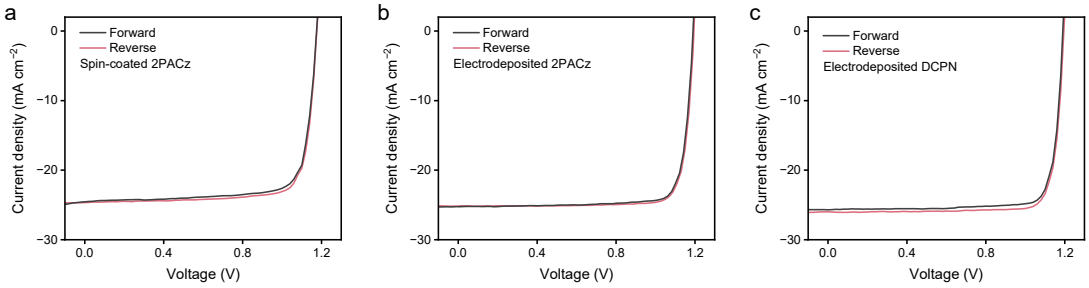

Supplementary Fig. 39. *J–V* curves (forward- and reverse-scan) of PSCs with different SAMs. (a) Spin-coated 2PACz. (b) Electrodeposited 2PACz. (c) Electrodeposited DCPN.

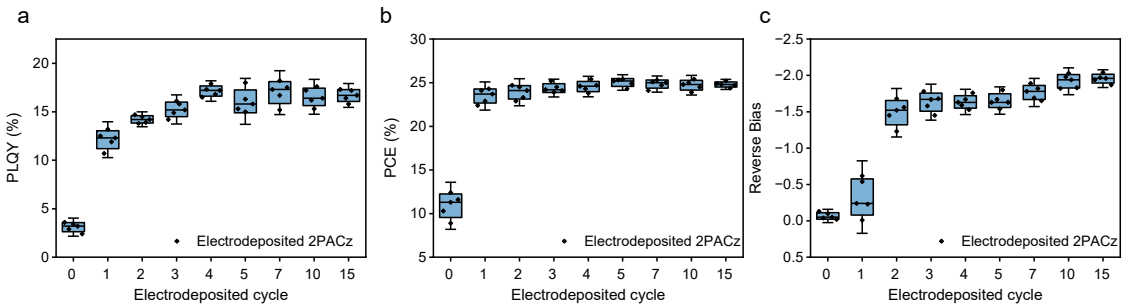

Supplementary Fig. 40. PLQY, PCE, and reverse-bias tolerance versus 2PACz electrodeposition cycle number. (a) Absolute external PLQY of perovskite films on ITO/electrodeposited 2PACz versus cycle number. (b) Device PCE versus cycle number. (c) Device reverse-bias tolerance (dark, single-direction sweep) versus cycle number (n=5). Gains are pronounced from cycles 1–5 and become statistically unchanged thereafter, consistent with IR-AFM coverage saturation and CV evolution; we therefore adopt 5 cycles as the standard condition.

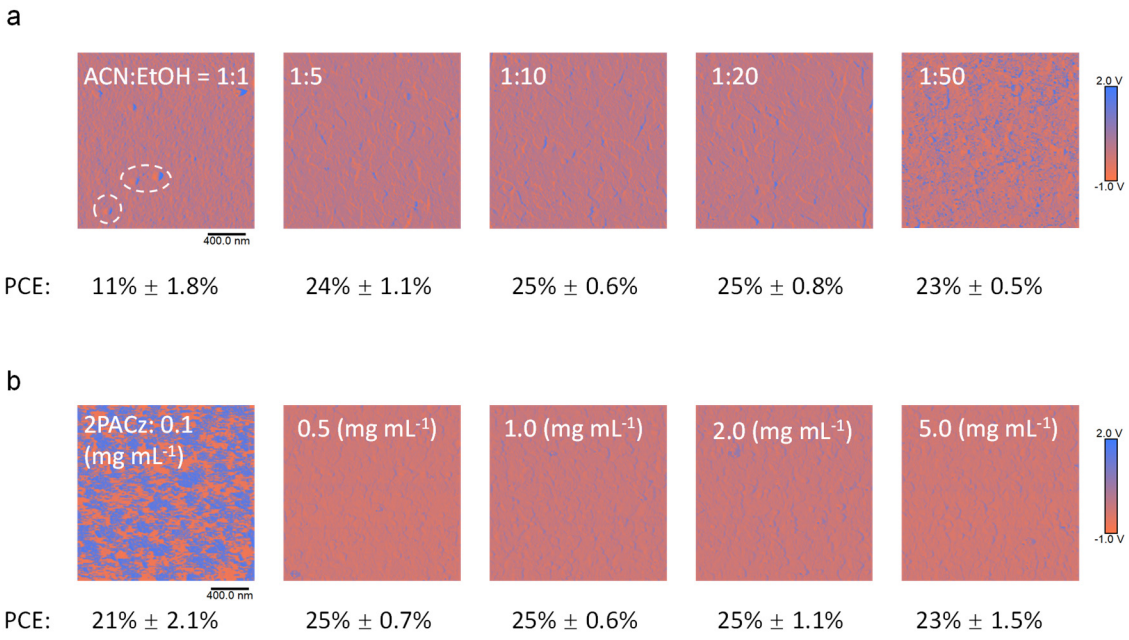

Supplementary Fig. 41. Effect of electrolyte solvent ratio and 2PACz concentration on ITO/electrodeposited 2PACz, probed by AFM phase maps. (a) Tuning the solvent ratio at fixed 2PACz = 1.0 mg mL^{-1}, $TBAPF_6$ = 0.10 M, and 5 cycles: ACN:EtOH = 1:1 showed particulates and non-uniform coverage; 1:50 exhibited inhomogeneity attributable to partial $TBAPF_6$ crystallization; and 1:5–1:20 were indistinguishable within AFM resolution and yielded comparable device PCE statistics. (b) Varying the 2PACz concentration at fixed ACN:EtOH = 1:10 (v/v), $TBAPF_6$ = 0.10 M, and 5 cycles: 0.1 mg mL^{-1} resulted in undercoverage within 5 cycles; 5.0 mg mL^{-1} showed slight aggregation and solubility limitations; and 0.5–2.0 mg mL^{-1} yielded homogeneous molecular layer with comparable device PCE statistics. Accordingly, we adopt a mixed solvent of ACN:EtOH = 1:10 (v/v) containing 2PACz = 1.0 mg mL^{-1} as the standard condition.

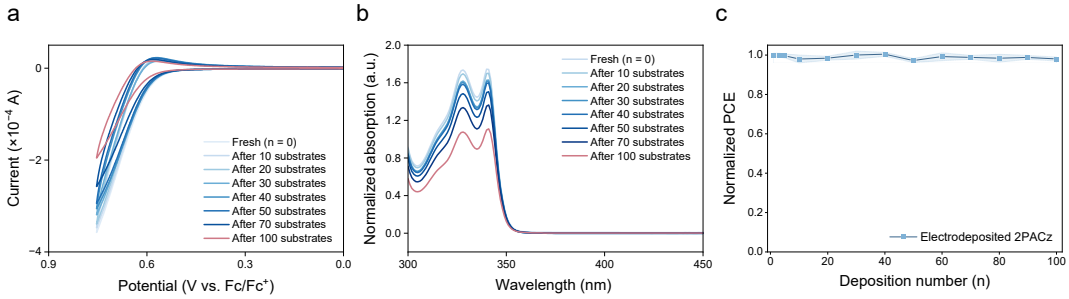

Supplementary Fig. 42. Evolution of electrolyte composition during sequential electrodeposition and correlation with device performance. (a) CV curves of the electrolyte reflecting 2PACz concentration, measured after every 10 substrates. (b) UV–vis absorption spectra of the electrolyte reflecting 2PACz concentration, measured after every 10 substrates. (c) Normalized PCE of devices fabricated from the corresponding substrate batches.

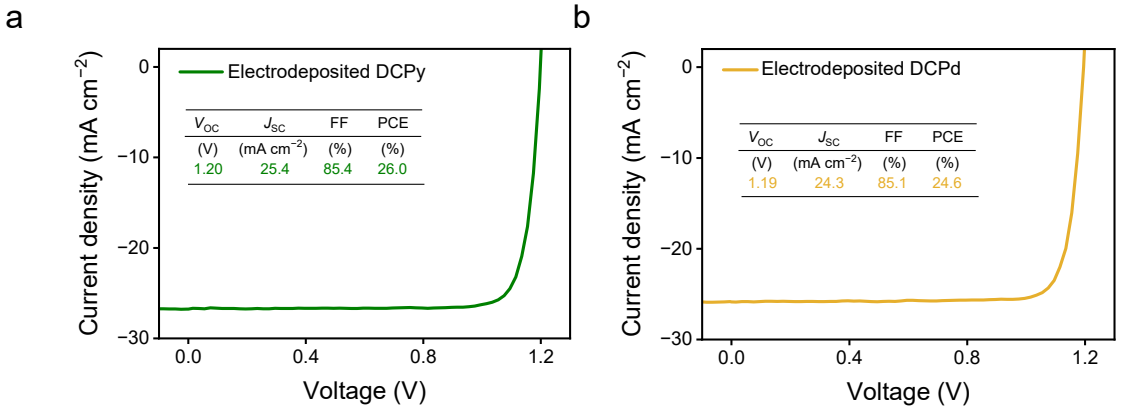

Supplementary Fig. 43. *J–V* characteristics and device metrics for perovskite cells with electrodeposited SAMs. (a) Electrodeposited DCPy. (b) Electrodeposited DCPd. Relative to electrodeposited 2PACz, DCPN tends to raise J_{SC}; DCPy yields small, reproducible gains in V_{OC} and FF; whereas DCPd shows a modest reduction in J_{SC} at comparable V_{OC}. These trends, observed across our device statistics, are consistent with terminal-group-dependent tuning of the contact and offer a practical handle for materials selection.

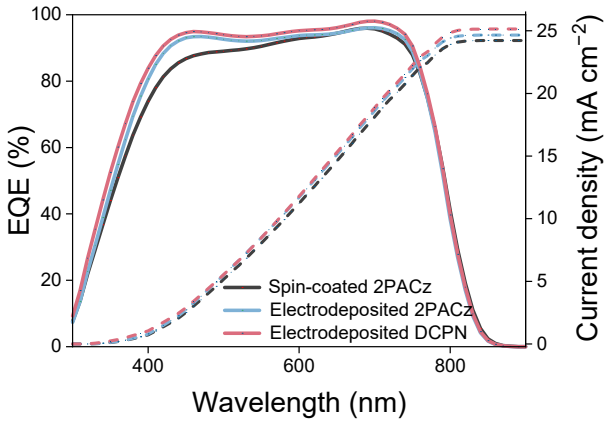

Supplementary Fig. 44. EQE spectra and EQE-integrated J_{SC} for PSCs with different SAMs.

华南国家计量测试中心
广东省计量科学研究院
SOUTH CHINA NATIONAL CENTER OF METROLOGY
GUANGDONG INSTITUTE OF METROLOGY

校 准 证 书
CALIBRATION CERTIFICATE

证书编号 NYX202500567 第 1 页，共 4 页
Certificate No. Page of

客户名称 华南理工大学
Name of the Customer South China University of Technology
联络信息 广东省广州市天河区五山路381号
Contact Information No.381,Wushan Road,Tianhe District,Guangzhou,Guangdong Province
计量器具名称 反式钙钛矿太阳电池
Description Inverted Perovskite Solar Cells
型号/规格 1.5 cm×1.5 cm
Model/Type
制造厂 华南理工大学
Manufacturer South China University of Technology
出厂编号 Z3-1 设备管理编号 ——
Serial No. Equipment No.
接收日期 2025 年 09 月 10 日
The date of receipt Y M D
校准日期 2025 年 09 月 10 日
The date of calibration Y M D
发布日期 2025 年 09 月 16 日
The date of issue Y M D

批 准 吴江宏
Authorized by
核 验 林鼎添
Reviewed by
校 准 梅书刚
Calibrated by

华南国家计量测试中心 证书专用章

扫一扫查真伪

实验室地址：中国广东省东莞市石排镇东国大道石排段152号 邮政编码：523343
电话：+8620 86594172 投诉电话：+8620 36611242 E-mail：scm@scm.com.cn
Add: No.152, Shipai Section, Dongguan Avenue, Shipai Town, Dongguan, Guangdong, China
Post Code:523343 Tel: +8620 86594172 Complaint Tel: +8620 36611242
证书真伪查询：www.scm.com.cn；cert.scm.com.cn Certificate Authenticity Identify: www.scm.com.cn；cert.scm.com.cn

5250912009 1

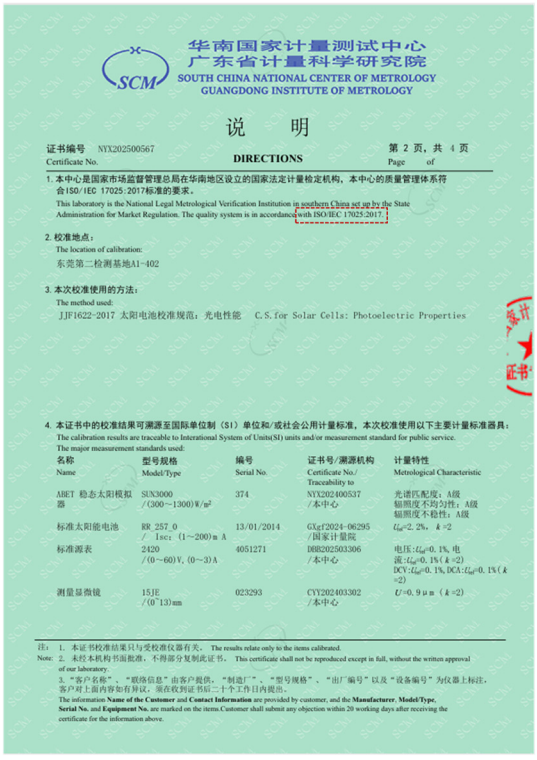

华南国家计量测试中心
广东省计量科学研究院
SOUTH CHINA NATIONAL CENTER OF METROLOGY
GUANGDONG INSTITUTE OF METROLOGY

说 明
DIRECTIONS

证书编号 NYX202500567 第 2 页，共 4 页
Certificate No. Page of

1. 本中心是国家市场监督管理总局在华南地区设立的国家法定计量检定机构，本中心的质量管理体系符合ISO/IEC 17025:2017标准的要求。
This laboratory is the National Legal Metrological Verification Institution in southern China set up by the State Administration for Market Regulation. The quality system is in accordance with ISO/IEC 17025:2017.

2. 校准地点：
The location of calibration:
东莞第二检测基地A1-402

3. 本次校准使用的方法：
The method used:
JJF1622-2017 太阳电池校准规范；光电性能 C.S. for Solar Cells: Photoelectric Properties

4. 本证书中的校准结果可溯源至国际单位制（SI）单位和/或社会公用计量标准，本次校准使用以下主要计量标准器具：
The calibration results are traceable to International System of Units(SI) units and/or measurement standard for public service.
The major measurement standards used:

名称 Name	型号规格 Model/Type	编号 Serial No.	证书号/溯源机构 Certificate No./ Traceability to	计量特性 Metrological Characteristic
ABET 稳态太阳模拟器	SUN3000 /(300～1300)W/m²	374	NYX202400537 /本中心	光谱匹配度：A级 辐照度不均匀性：A级 辐照度不稳性：A级
标准太阳能电池	RR_257_0 /Isc：(1～200)mA	13/01/2014	GXgf2024-06295 /国家计量院	U_{rel}=2.2%，k=2
标准源表	2420 /(0～60)V，(0～3)A	4051271	DBB202503306 /本中心	电压：U_{rel}=0.1%，电流：U_{rel}=0.1%（k=2） DCV：U_{rel}=0.1%，DCA：U_{rel}=0.1%（k=2）
测量显微镜	15JE /(0～13)mm	023293	CYJ202403302 /本中心	U=0.9μm（k=2）

注： 1. 本证书校准结果只与受校准仪器有关， The results relate only to the items calibrated.
Note: 2. 未经本机构书面批准，不得部分复制此证书， This certificate shall not be reproduced except in full, without the written approval of our laboratory.
3. “客户名称”、“联络信息”由客户提供，“制造厂”、“型号规格”、“出厂编号”以及“设备编号”为仪器上标注，客户对上面内容如有异议，须在收到证书后二十个工作日内提出。
The information Name of the Customer and Contact Information are provided by customer, and the Manufacturer, Model/Type, Serial No. and Equipment No. are marked on the items.Customer shall submit any objection within 20 working days after receiving the certificate for the information above.

华南国家计量测试中心
广东省计量科学研究院
SOUTH CHINA NATIONAL CENTER OF METROLOGY
GUANGDONG INSTITUTE OF METROLOGY

校 准 结 果
RESULTS OF CALIBRATION

证书编号 NYX202500567 原始记录号 NYX202500567 第 4 页，共 4 页
Certificate No. Record No. Page of

5、被测样品信息：
Sample information:

图2 测试中使用的掩膜板及被测样品正面照片
Figure 2 Mask used during measurement and obverse side of the sample

图3 被测样品反面照片
Figure 3 Reverse side of the sample

金属掩膜板光阑平均尺寸： 2.085 mm ×2.090mm
The average size of metal aperture mask:

说明(Note)：
1、被测样品的有效辐照面积基于对金属掩模板光阑的测量。
The effective illuminated area of the measured sample based on the measurement of metal aperture mask.
2、本次测量结果的扩展不确定度为：开路电压V_{oc}：U_{rel}=1.2%，短路电流I_{sc}：U_{rel}=2.7%，最大功率P_{max}：U_{rel}=3.0%，转换效率η：U_{rel}=3.4%，(k=2)。
The expanded uncertainty of measuring results: V_{oc}: U_{rel}=1.2%, I_{sc}: U_{rel}=2.7%, P_{max}: U_{rel}=3.0%, η: U_{rel}=3.4%, (k=2).
3、校准活动中对测量结果有影响的条件：温度:(25±2)℃，湿度:(40±5)%RH。
Conditions under which the calibrations were made that have an influence on the measurement results: Temperature:(25±2)℃, Humidity:(40±5)%RH.
4、本证书中给出的扩展不确定度依据JJF1059.1-2012《测量不确定度评定与表示》评定，由合成标准不确定度乘以包含概率约为95%时对应的包含因子k得到。
The expanded uncertainty given in this certificate is evaluated according to JJF 1059.1-2012 *Evaluation and Expression of Uncertainty in Measurement*, which is obtained by multiplying the combined standard uncertainty by the coverage factor k corresponding to the coverage probability of about 95%.
5、该仪器的溯源日期为本证书的“校准日期”，由于复校时间间隔的长短是由仪器的使用情况、使用者、仪器本身质量等诸因素所决定的，因此，送检单位可根据实际使用情况自主决定复校时间间隔。更换重要部件、维修或对仪器性能有怀疑时，应及时校准。
The traceability date of this instrument is the “Calibration Date” on this certificate, Since the calibration interval is determined by the use of the instrument,operation of the user, the quality of the instrument itself and other factors, the re-calibration date can decided by the user according to the actual situation.In case of replacement of important parts,maintenance or doubt on the performance of the instrument,it shall be calibrated in time.

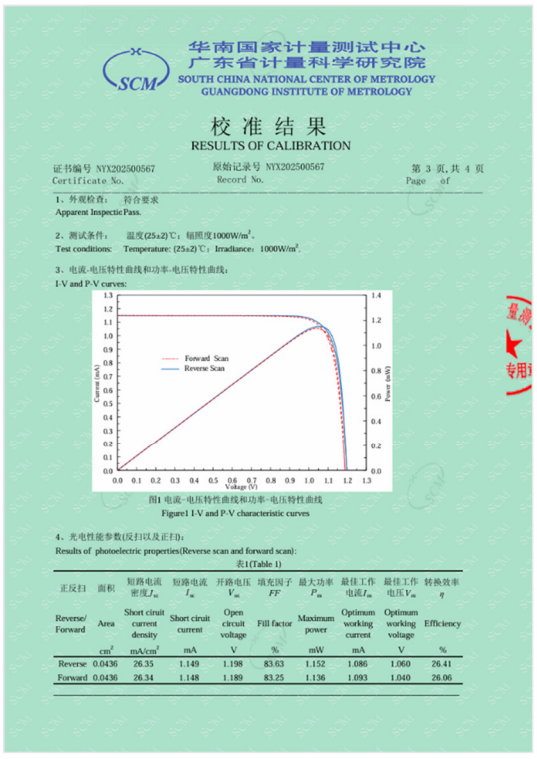

华南国家计量测试中心
广东省计量科学研究院
SOUTH CHINA NATIONAL CENTER OF METROLOGY
GUANGDONG INSTITUTE OF METROLOGY

校 准 结 果
RESULTS OF CALIBRATION

证书编号 NYX202500567 原始记录号 NYX202500567 第 3 页，共 4 页
Certificate No. Record No. Page of

1、外观检查： 符合要求
Apparent Inspectic Pass.

2、测试条件： 温度(25±2)℃；辐照度1000W/m²。
Test conditions: Temperature: (25±2)℃; Irradiance：1000W/m².

3、电流-电压特性曲线和功率-电压特性曲线：
I-V and P-V curves:

图1 电流-电压特性曲线和功率-电压特性曲线
Figure1 I-V and P-V characteristic curves

4、光电性能参数(反扫以及正扫)：
Results of photoelectric properties(Reverse scan and forward scan):
表1(Table 1)

正反扫 Reverse/ Forward	面积 Area	短路电流密度J_{sc} Short circuit current density	短路电流I_{sc} Short circuit current	开路电压V_{oc} Open circuit voltage	填充因子FF Fill factor	最大功率P_m Maximum power	最佳工作电流I_m Optimum working current	最佳工作电压V_m Optimum working voltage	转换效率η Efficiency
	cm^2	mA/cm^2	mA	V	%	mW	mA	V	%
Reverse	0.0436	26.35	1.149	1.198	83.63	1.152	1.086	1.060	26.41
Forward	0.0436	26.34	1.148	1.189	83.25	1.136	1.093	1.040	26.06

Supplementary Fig. 45. Certified performance of perovskite solar cells with electrodeposited DCPN. Certified by an ISO/IEC 17025:2017-accredited third-party testing center.

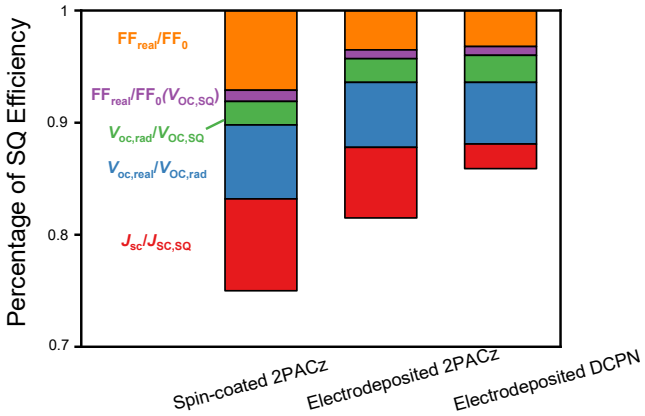

Supplementary Fig. 46. Shockley–Queisser loss accounting for SAM contacts. Stacked contributions to η_{real}/η_{SQ} for spin-coated 2PACz, electrodeposited 2PACz, and electrodeposited DCPN. The multiplicative factors are, in order: $\left(J_{sc}/J_{SC}^{SQ}\right)$, $\left(V_{OC,rad}/V_{OC}^{SQ}\right)$, $\left(V_{OC,real}/V_{OC,rad}\right)$, $\left(FF_0\left(V_{OC,real}\right)/FF_0\left(V_{OC,SQ}\right)\right)$, and $\left(FF_{real}/FF_0\left(V_{OC,real}\right)\right)$.

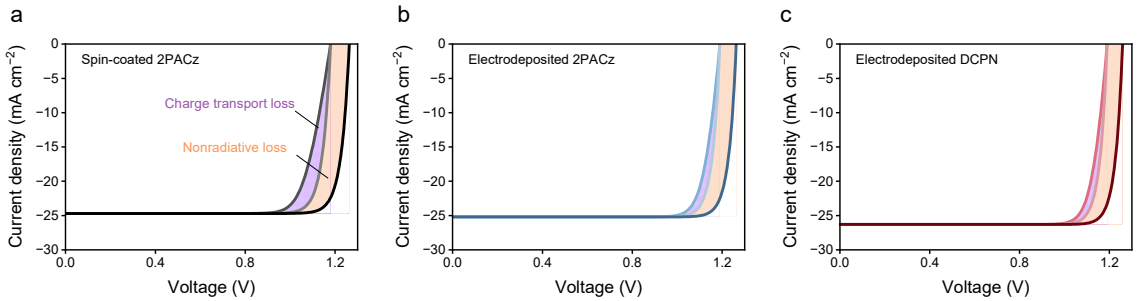

Supplementary Fig. 47. Pseudo *J–V* decomposition isolating non-radiative and transport losses. (a) spin-coated 2PACz. (b) electrodeposited 2PACz. (c) electrodeposited DCPN.

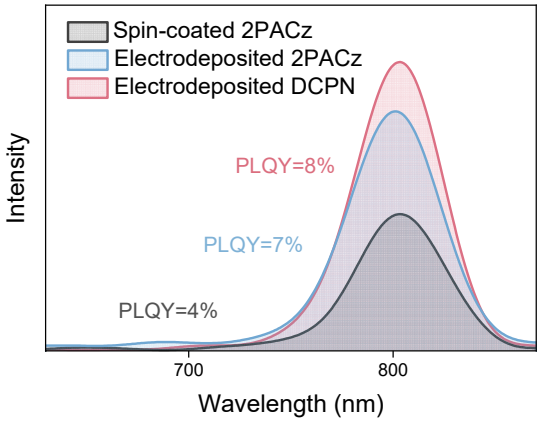

Supplementary Fig. 48. Device absolute PLQY of complete perovskite solar cells with different SAMs.

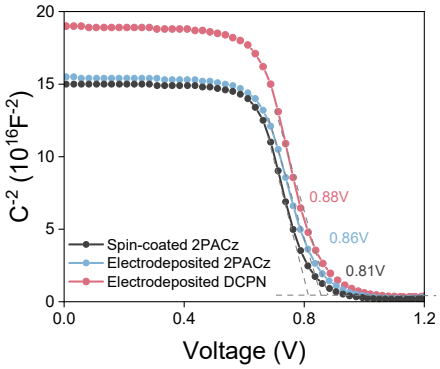

Supplementary Fig. 49. Mott-Schottky analysis (C–V) of perovskite solar cells with different SAMs. $1/C^2$–V plots obtained from capacitance–voltage measurements and linear-fit regions used to extract the built-in potential.

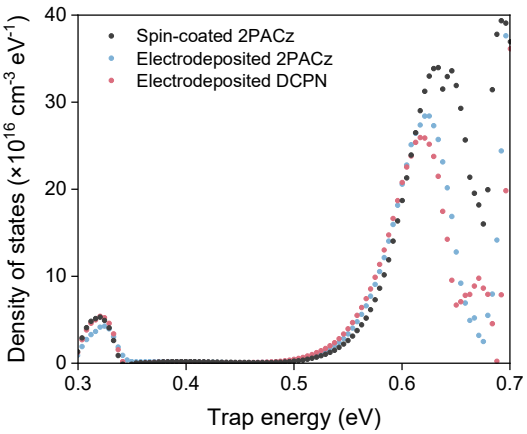

Supplementary Fig. 50. Capacitance-derived trap-state distribution (trap DOS) in perovskite solar cells with different SAMs**.**

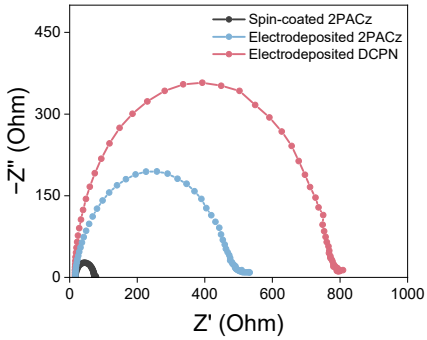

Supplementary Fig. 51. Nyquist analysis (EIS) of perovskite solar cells with different SAMs.

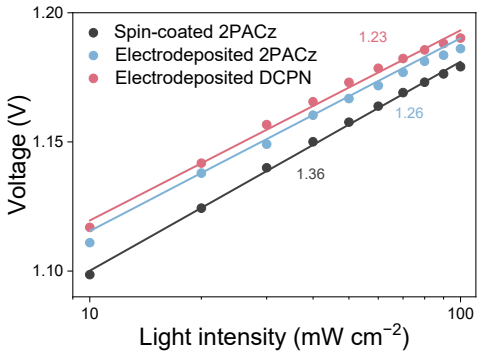

Supplementary Fig. 52. Light-intensity dependence of V_{OC} for perovskite solar cells with different SAMs.

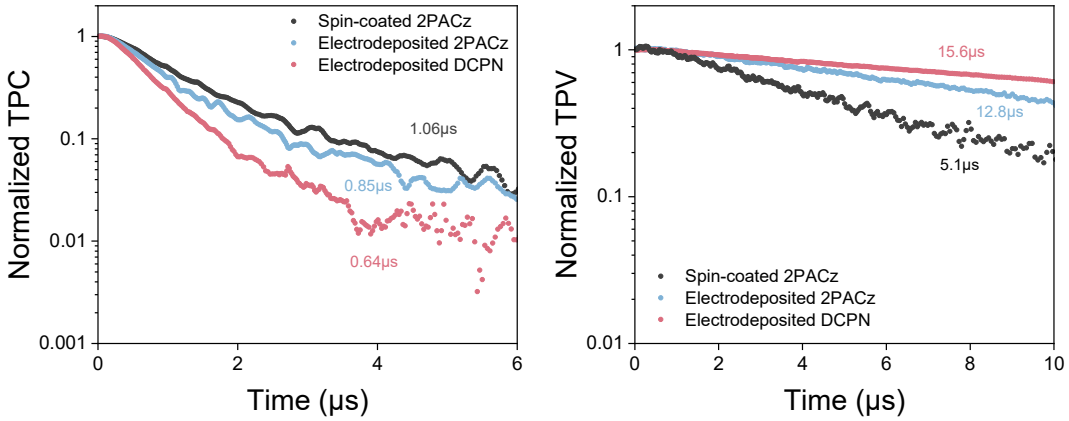

Supplementary Fig. 53. Transient photocurrent (TPC) and transient photovoltage (TPV) of perovskite solar cells with different SAMs.

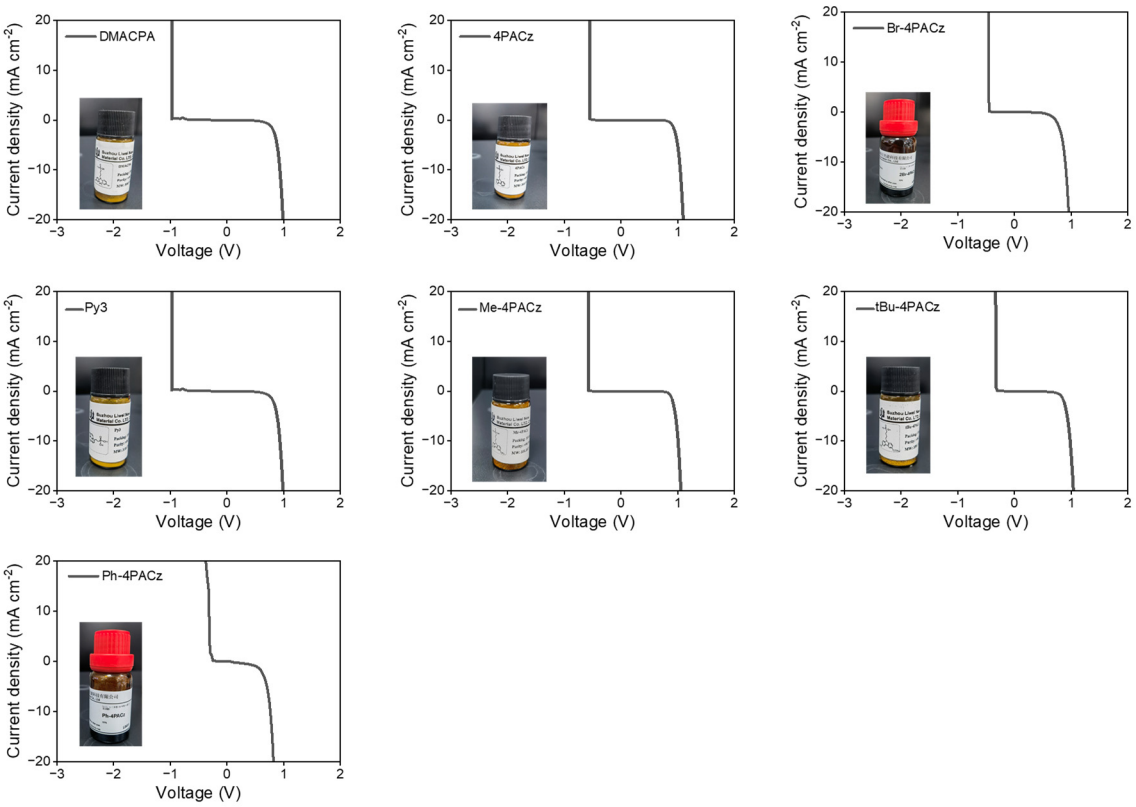

Supplementary Fig. 54. Dark *J–V* revealing distinct reverse-bias behaviors across devices with various SAMs.

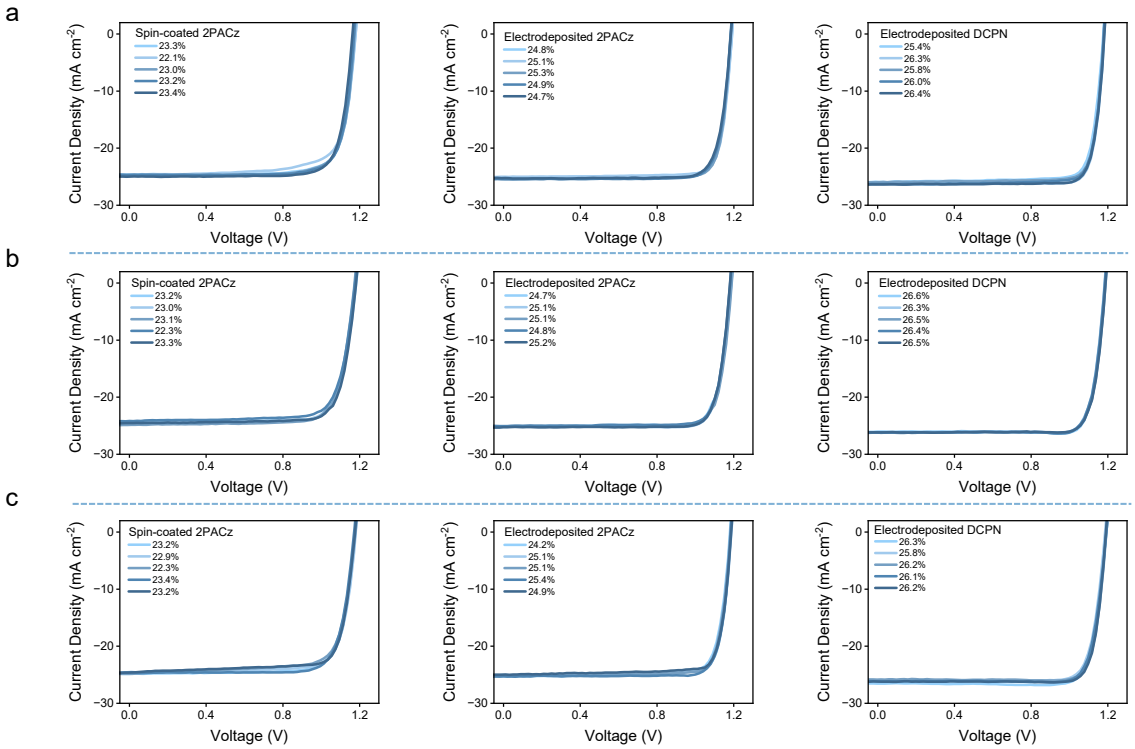

Supplementary Fig. 55. Initial *J–V* characteristics and PCE values of devices used for stability testing. Initial device performance of cells subjected to (a) dark-storage ageing, (b) MPP-tracking stability testing and (c) open-circuit ageing.

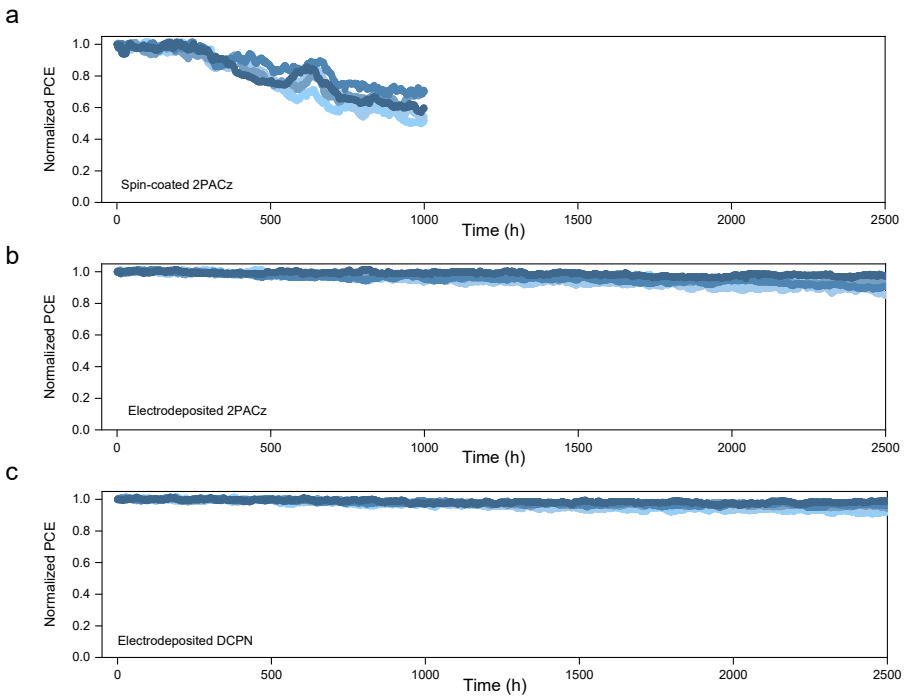

Supplementary Fig. 56. Individual MPP-tracking traces of devices under one-sun-equivalent illumination at 65 °C in a nitrogen-filled glovebox. Individual normalized PCE evolution curves of five devices based on (a) spin-coated 2PACz, (b) electrodeposited 2PACz and (c) electrodeposited DCPN during continuous MPP tracking at 65 °C under one-sun-equivalent illumination in a nitrogen-filled glovebox.

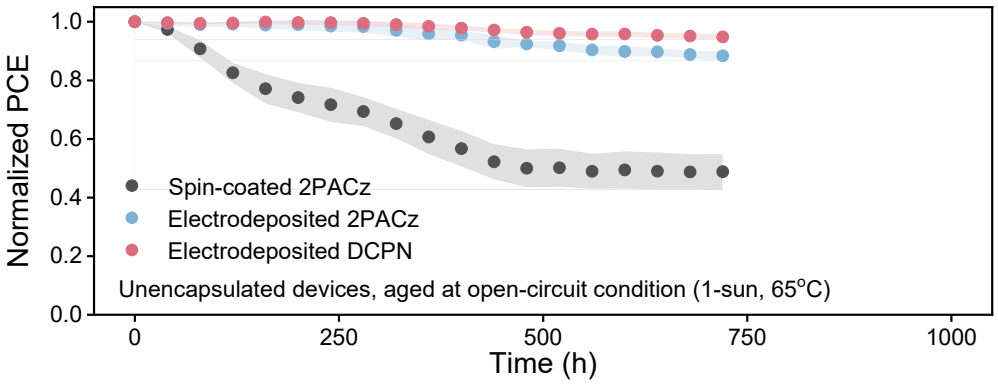

Supplementary Fig. 57. Open-circuit ageing of devices at 65 °C under one-sun-equivalent illumination. Normalized PCE evolution of devices based on spin-coated 2PACz, electrodeposited 2PACz and electrodeposited DCPN aged under these open-circuit conditions in a nitrogen-filled glovebox.

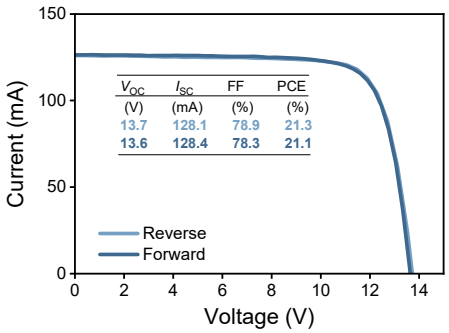

Supplementary Fig. 58. *J–V* curves and photovoltaic parameters of the 65 cm^2 module with electrodeposited SAM (reverse/forward scans).

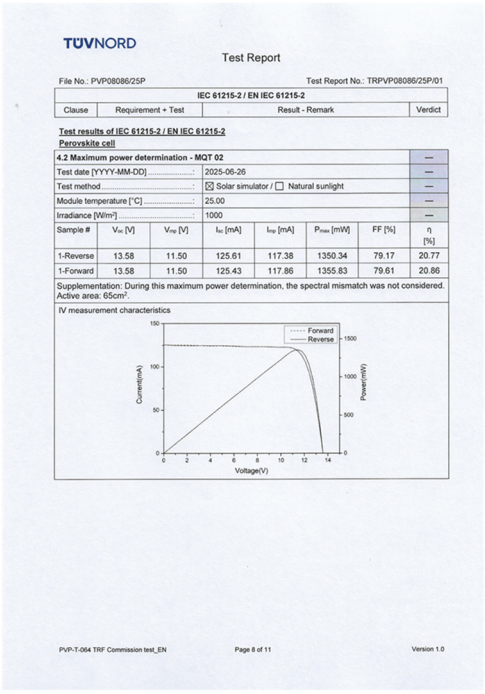

TÜVNORD

Test Report

File No.: PVP08086/25P Test Report No.: TRPVP08086/25P/01

IEC 61215-2 / EN IEC 61215-2			
Clause	Requirement + Test	Result - Remark	Verdict

Test results of IEC 61215-2 / EN IEC 61215-2

Perovskite cell

4.2 Maximum power determination - MQT 02							----
Test date [YYYY-MM-DD]	:	2025-06-26					----
Test method	:	☒ Solar simulator / ☐ Natural sunlight					----
Module temperature [°C]	:	25.00					----
Irradiance [W/m²]	:	1000					----

Sample #	V_{oc} [V]	V_{mp} [V]	I_{sc} [mA]	I_{mp} [mA]	P_{max} [mW]	FF [%]	η [%]
1-Reverse	13.58	11.50	125.61	117.38	1350.34	79.17	20.77
1-Forward	13.58	11.50	125.43	117.86	1355.83	79.61	20.86

Supplementation: During this maximum power determination, the spectral mismatch was not considered. Active area: 65cm².

IV measurement characteristics

PVP-T-064 TRF Commission test_EN Page 8 of 11 Version 1.0

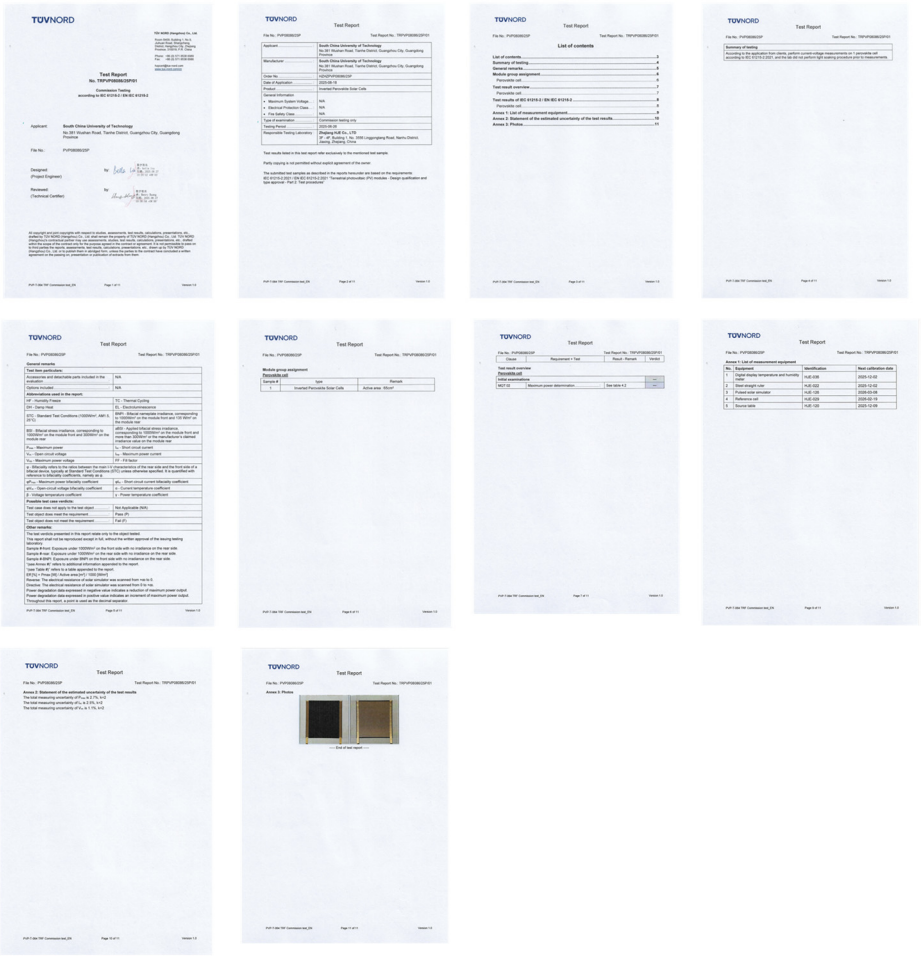

Supplementary Fig. 59. TÜV certification report for a 65 cm^2 PSC module with electrodeposited SAMs, tested in accordance with IEC 61215-2:2021.

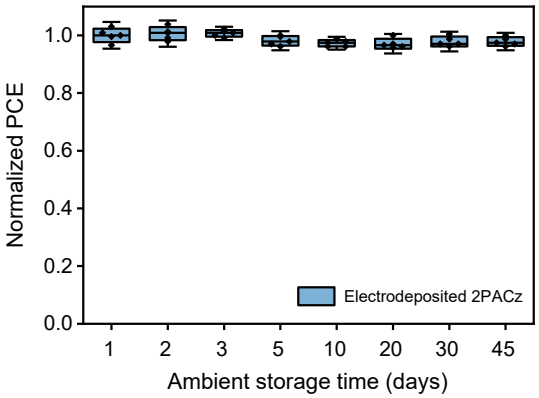

Supplementary Fig. 60. PCE statistics of PSCs, in which the electrodeposited 2PACz substrates were stored in ambient air for different durations before perovskite deposition. The statistics show that the devices retain 98% of the initial PCE even after 45 days, evidencing the stability of the electrodeposited molecular layer and supporting a pre-staged manufacturing flow (mean ± s.d.; n=5).

Supplementary Table 1. Mean current and H_2 Faradaic efficiency from controlled-potential electrolysis of blank electrolyte and 2PACz solutions (mean ± s.d.; n=3).

Sample	Current ($\times 10^{-4}$ A)	Faradaic Efficiency for Hydrogen Evolution(%)
Blank electrolyte	0.18 ± 0.04	0
2PACz (1mg mL^{-1})	0.57 ± 0.02	78.7 ± 6.3
2PACz (10mg mL^{-1})	1.35 ± 0.10	~100

Supplementary Table 2. Photovoltaic parameters of devices fabricated with different SAMs. Average device characteristics with standard deviation were obtained based on 10 cells (mean ± s.d.; n=10).

Device	V_{OC} (V)	J_{SC} (mA cm^{-2})	FF(%)	PCE(%)
Spin-coated 2PACz	1.17 ± 0.01	24.4 ± 0.4	80.3 ± 0.6	22.9 ± 0.3
Electrodeposited 2PACz	1.18 ± 0.01	25.1 ± 0.1	84.0 ± 0.7	25.0 ± 0.4
Electrodeposited DCPN	1.19 ± 0.00	26.1 ± 0.2	85.5 ± 0.5	26.4 ± 0.2

Supplementary Table 3. Five-factor Shockley–Queisser loss accounting.

Device	$\frac{\eta_{real}}{\eta_{SQ}}$(%)	$\frac{J_{SC}}{J_{SC}^{SQ}}$(%)	$\frac{V_{OC}^{real}}{V_{OC}^{rad}}$(%)	$\frac{V_{OC}^{rad}}{V_{OC}^{SQ}}$(%)	$\frac{FF(V_{OC}^{real})}{FF(V_{OC}^{SQ})}$(%)	$\frac{FF_{real}}{FF(V_{OC}^{real})}$(%)
Spin-coated 2PACz	77.3	91.8	93.4	97.9	99.0	92.9
Electrodeposited 2PACz	82.7	93.7	94.2	97.9	99.2	96.5
Electrodeposited DCPN	86.6	97.8	94.5	97.6	99.2	96.8

Supplementary Table 4. Pseudo–*J–V* analysis: inputs and extracted metrics at 1 sun.

Sample		*V*oc (V)	*J*sc (mA cm^{-2})	FF (%)	PCE (%)
Spin-coated 2PACz	Measured *J–V*	1.18	24.7	80.7	23.4
	Pseudo *J–V* (no transport)	1.18	24.7	86.9	25.4
	Pseudo *J–V* (radiative-limit)	1.26	24.7	86.9	27.1
Electrodeposited 2PACz	*J–V*	1.19	25.2	84.6	25.4
	Pseudo *J–V* (no transport)	1.19	25.2	87.7	26.3
	Pseudo *J–V* (radiative-limit)	1.26	25.2	87.7	27.8
Electrodeposited DCPN	*J–V*	1.19	26.3	85.1	26.8
	Pseudo *J–V* (no transport)	1.19	26.3	87.9	27.5
	Pseudo *J–V* (radiative-limit)	1.26	26.3	87.9	29.0

Supplementary Table 5. Summary of operational stability and reverse-bias breakdown tolerance for PSCs with different SAMs. Reported operational-stability values were collected from the cited literature, whereas reverse-bias breakdown voltages were measured under the same dark *J–V* protocol in this work (mean ± s.d.; n=5).

SAMs	Stability after 1000 h (%)	Reverse breakdown Voltage (V)	Ref.
MeO-4PACz	79	−0.73±0.07	3, 4
Ph-4PACz	86	−0.42±0.05	5
DMACPA	95	−1.02±0.09	6
4PACz	53	−0.58±0.07	7
Br-4PACz	93	−0.49±0.05	8
Py3	97	−0.97±0.09	9
Me-4PACz	80	−0.63±0.06	10
tBu-4PACz	90	−0.37±0.04	11
Spin-coated 2PACz	71	−0.51±0.03	-
Electrodeposited 2PACz	98	−1.67±0.09	-
Electrodeposited DCPN	99	−2.5±0.10	-

Supplementary Table 6. Photovoltaic parameters of PSC modules with electrodeposited SAMs. Average device characteristics with standard deviation were obtained based on 5 modules (mean ± s.d.; n = 5).

Device		V_{OC} (V)	I_{SC} (mA)	**FF(%)**	**PCE(%)**
65cm^2 perovskite module	Best	13.7	128.1	78.9	21.3
	Average	13.6±0.14	127.4±2.18	77.64±1.07	20.7±0.25

References and Notes

1. Lu, T. & Chen, F. Multiwfn: A multifunctional wavefunction analyzer. *J. Comput. Chem.* **33**, 580–592 (2012).
2. Liu, Z., Lu, T. & Chen, Q. Intermolecular interaction characteristics of the all-carboatomic ring, cyclo[18]carbon: Focusing on molecular adsorption and stacking. *Carbon* **165**, 461–470 (2020).
3. Jiang, F. et al. Improved reverse bias stability in p–i–n perovskite solar cells with optimized hole transport materials and less reactive electrodes. Nat. Energy **9**, 1275–1284 (2024).
4. Liu, M. *et al.* Defect-passivating and stable benzothiophene-based self-assembled monolayer for high-performance inverted perovskite solar cells. *Adv. Energy Mater.* **14**, 2303742 (2024).
5. Sun, A. *et al.* High open-circuit voltage (1.197 V) in large-area (1 cm^2) inverted perovskite solar cells via interface planarization and a highly polar self-assembled monolayer. *Adv. Energy Mater.* **14**, 2303941 (2024).
6. Tan, Q. et al. Inverted perovskite solar cells using dimethylacridine-based dopants. Nature 620, 545–551 (2023).
7. Huang, Y. *et al.* Asymmetric modification of carbazole-based self-assembled monolayers by a hybrid strategy for inverted perovskite solar cells. *Angew. Chem. Int. Ed.* **64**, e202416188 (2025).
8. Peng, W. et al. A versatile energy-level-tunable hole-transport layer for multi-composition inverted perovskite solar cells. Energy Environ. Sci. **18**, 874–883 (2025).
9. Zhao, K. et al. peri-Fused polyaromatic molecular contacts for perovskite solar cells. *Nature* **632**, 301–306 (2024).
10. Qu, G. et al. Conjugated linker-boosted self-assembled monolayer molecule for inverted perovskite solar cells. Joule **8**, 2123–2134 (2024).
11. Su, Z. *et al.* Stereo-hindrance-induced conformal self-assembled monolayer for high-efficiency inverted perovskite solar cells. *Small* **20**, e2407387 (2024).